

Hints of a Sulfur-rich Atmosphere around the $1.6 R_{\oplus}$ Super-Earth L98-59 d from JWST NIRspec G395H Transmission Spectroscopy

Amélie Gressier¹ , Néstor Espinoza^{1,2} , Natalie H. Allen² , David K. Sing^{3,4} , Agnibha Banerjee⁵ , Joanna K. Barstow⁵ , Jeff A. Valenti¹ , Nikole K. Lewis⁶ , Stephan M. Birkmann⁷ , Ryan C. Challener⁸ , Elena Manjavacas^{3,9} ,

Catarina Alves de Oliveira⁷ , Nicolas Crouzet¹⁰ , and Tracy. L Beck¹ 

¹ Space Telescope Science Institute, 3700 San Martin Drive, Baltimore, MD 21218, USA

² William H. Miller III Department of Physics and Astronomy, Johns Hopkins University, Baltimore, MD 21218, USA

³ Department of Physics and Astronomy, Johns Hopkins University, 3400 N. Charles Street, Baltimore, MD 21218, USA

⁴ Department of Earth and Planetary Sciences, Johns Hopkins University, 3400 N. Charles Street, Baltimore, MD 21218, USA

⁵ School of Physical Sciences, The Open University, Milton Keynes, MK7 6AA, UK

⁶ Department of Astronomy and Carl Sagan Institute, Cornell University, 122 Sciences Drive, Ithaca, NY 14853, USA

⁷ European Space Agency, European Space Astronomy Centre, Camino Bajo del Castillo s/n, E-28692 Villanueva de la Cañada, Madrid, Spain

⁸ Department of Astronomy, Cornell University, 122 Sciences Drive, Ithaca, NY 14853, USA

⁹ AURA for the European Space Agency (ESA), ESA Office, Space Telescope Science Institute, 3700 San Martin Drive, Baltimore, MD 21218, USA

¹⁰ Leiden Observatory, Leiden University, P.O. Box 9513, 2300 RA Leiden, The Netherlands

Received 2024 May 29; revised 2024 August 23; accepted 2024 August 25; published 2024 October 30

Abstract

Detecting atmospheres around planets with a radius below $1.6 R_{\oplus}$, commonly referred to as rocky planets, has proven to be challenging. However, rocky planets orbiting M dwarfs are ideal candidates due to their favorable planet-to-star radius ratio. Here, we present one transit observation of the Super-Earth L98-59 d ($1.58 R_{\oplus}$ and $2.31 M_{\oplus}$), at the limit of rocky/gas-rich, using the JWST NIRSpec G395H mode covering the 2.8 – $5.1 \mu\text{m}$ wavelength range. The extracted transit spectrum from a single transit observation deviates from a flat line by 2.6σ – 5.6σ , depending on the data reduction and retrieval setup. The hints of an atmospheric detection are driven by a large absorption feature between 3.3 and $4.8 \mu\text{m}$. A stellar contamination retrieval analysis rejected the source of this feature as being due to stellar inhomogeneities, making the best fit an atmospheric model including sulfur-bearing species, suggesting that the atmosphere of L98-59 d may not be at equilibrium. This result will need to be confirmed by the analysis of the second NIRSpec G395H visit in addition to the NIRISS SOSS transit observation.

Unified Astronomy Thesaurus concepts: Exoplanet atmospheres (487); Exoplanet atmospheric composition (2021); Transmission spectroscopy (2133); Astronomy data reduction (1861); Planetary atmospheres (1244); Stellar atmospheres (1584); Infrared spectroscopy (2285); Super Earths (1655); Extrasolar rocky planets (511)

Materials only available in the [online version of record](#): data behind figures, machine-readable table

1. Introduction

Pushing the instrumental limit to possibly detect an atmosphere around an Earth-like planet is the first step in understanding whether any of these planets could support life and to what extent we could detect it. The large planet-to-star radius ratio, coupled with the high frequency of the transit event, creates favorable conditions for searching for an atmosphere using transmission spectroscopy around planets orbiting M dwarfs. However, in the search for an atmospheric signal around a rocky planet, one must balance the M dwarf opportunity with the possibility that long exposure to X-ray and EUV radiations can strip away the atmosphere (J. E. Owen & Y. Wu 2013; J. E. Owen 2019). Besides, M dwarf stars can mimic planetary atmospheric features in the transmission spectrum from photospheric inhomogeneities, known as stellar contamination (B. V. Rackham et al. 2018).

Space- and ground-based observations of rocky planets ($R_p < 1.6 R_{\oplus}$) have not yet provided strong and compelling evidence of atmospheric signals. The Hubble Space Telescope Wide Field Camera 3 Grism 141 (HST WFC3 G141), widely

used in transmission spectroscopy for its water band at $1.4 \mu\text{m}$, did not yield conclusive and/or significant evidence due to its precision and limited spectral range (J. de Wit et al. 2016, 2018; H. R. Wakeford et al. 2019; A. Gressier et al. 2022; B. Edwards et al. 2021; L. V. Mugnai et al. 2021; L. J. Garcia et al. 2022). Similarly, no strong constraints were found using ground-based (H. Diamond-Lowe et al. 2018) and Spitzer observations (B.-O. Demory et al. 2011, 2012, 2015, 2016; L. Kreidberg et al. 2019; I. J. M. Crossfield et al. 2022; S. Zieba et al. 2022).

The atmospheric features in transmission for warm rocky planets are expected to reach 20–100 ppm, which approaches the expected noise floor of the James Webb Space Telescope instruments (T. P. Greene et al. 2016). Even for the JWST, detecting an atmosphere around a terrestrial world is a challenge, and this has been confirmed within the first years of observations. To date, no strong evidence for an atmosphere around a rocky exoplanet has been found (S. E. Moran et al. 2018; E. M. May et al. 2023; J. Lustig-Yaeger et al. 2023; J. Kirk et al. 2024). TRAPPIST-1 b and c photometric data points and transmission spectra are so far consistent with no or small atmospheric signals, with the interpretation of the transmission spectrum complicated by the presence of significant stellar contamination (O. Lim et al. 2023; S. Zieba et al. 2023; T. P. Greene et al. 2023).

The L98-59 system is composed of three rocky transiting planets (R. Cloutier et al. 2019; V. B. Kostov et al. 2019), with



Original content from this work may be used under the terms of the [Creative Commons Attribution 4.0 licence](#). Any further distribution of this work must maintain attribution to the author(s) and the title of the work, journal citation and DOI.

radii below $1.58 R_{\oplus}$, and a nontransiting planet (O. D. S. Demangeon et al. 2021) orbiting a bright M3 dwarf ($K = 7.01$ mag). Spanning the HST and JWST cycles 1 and 2, the L98-59 system stands out as one of the most extensively studied multiplanetary systems in emission and transmission spectroscopy (cycle 1 General Observation, GO, and Guaranteed Time Observation, GTO, programs 1201, 1224, and 2512 and cycle 2 GO 3942, 3730, and 4098). So far, the HST WFC3 G141 observations in the 1.1 – $1.7 \mu\text{m}$ range have not provided strong evidence of an atmosphere for any planets in the system. Both M. Damiano et al. (2022) for planet b and L. Zhou et al. (2023) for planets c and d rejected cloud-free hydrogen and helium atmospheres. However, they could not rule out primary cloudy/hazy or water-rich atmospheres.

Here, we present the result of the JWST-GTO-1224 program observations of the third planet of the system, L98-59 d, consisting of one transit covering the 2.87 – $5.17 \mu\text{m}$ wavelength range. With a radius of $1.58 \pm 0.08 R_{\oplus}$ and a mass of $2.31^{+0.46}_{-0.45} M_{\oplus}$ (R. Luque & E. Palle 2022), L98-59 d lies on the boundary defined by L. A. Rogers (2015) between rocky and gas-rich planets, making it a highly intriguing target. In this Letter, we first present the observations in Section 2. In Section 3, we detail the two independent data analyses used to extract the transmission spectrum. Section 4 describes the interpretations we carried out, including atmospheric and stellar contamination forward and retrieval modeling (Table 1). We discuss the results in the final Section 5.

2. JWST Observations of L98-59 d

We observed one transit of L98-59 d using the NIRSpec/G395H mode as part of the JWST GTO cycle 1 Program 1224, led by PI Stephan Birkmann. The G395H instrument mode covers the wavelength range from 2.87 to $5.17 \mu\text{m}$, at a native resolution of $R \sim 2700$. The grating is split over two detectors NRS1 and NRS2, with a gap between 3.72 and $3.82 \mu\text{m}$. The observations started on 2023 June 25, and covered the full transit and sufficient baseline for a total of 5.34 hr, resulting in 2121 integrations, each composed of six groups up the ramp. The observation used the NIRSpec Bright Object Time Series mode with the NRSRAPID readout pattern, S1600A1 slit, and the SUB2048 subarray.

3. Data Reduction

The reduction of L98-59 d NIRSpec G395H observations was obtained using two independent pipelines, `transitspectroscopy` (N. Espinoza 2022) and `FIREFLY` (Z. Rustamkulov et al. 2022, 2023), which have already been benchmarked for the JWST Early Release Science (ERS) program (L. Alderson et al. 2023; Z. Rustamkulov et al. 2023). `FIREFLY` has provided data reductions for smaller planets observations with the JWST NIRSpec G395H (E. M. May et al. 2023; J. Lustig-Yaeger et al. 2023; S. E. Moran et al. 2023), which makes it a good comparison.

3.1. Data Reduction with `transitspectroscopy`

We used the `jwst` pipeline version 1.12.5 and the `transitspectroscopy` pipeline (N. Espinoza 2022)¹¹ to reduce the NIRSpec G395H transit of L98-59 d. The reduction process followed the `jwst` pipeline from `uncal.fits` to `rateints`.

fits, excluding the jump step detection, which we customized using the `transitspectroscopy` algorithm. This algorithm identifies outliers at the pixel level within each group by calculating group differences, applying a median filter, and detecting jumps. Spectral tracing was performed using the `trace_spectrum` function, smoothed with a spline function. We determined the trace position using a cross-correlation method with a Gaussian input, covering specified pixel ranges for NRS1 and NRS2. Background estimation involved masking pixels around the trace and calculating the median of the remaining pixels. To address $1/f$ noise (P. Jakobsen et al. 2022; S. M. Birkmann et al. 2022)—noise arising from the electronics of the readout pattern, which appears as column striping in the subarray image—we subtracted the median out-of-transit frame and iteratively removed the median of nonomitted pixels near the trace position. The stellar spectrum was extracted using the `getSimpleSpectrum` routine with a 3-pixel radius aperture, minimizing out-of-transit flux. We employed a box-extraction method to sum flux within the aperture and replaced outliers exceeding a 5σ threshold with a 1D median filter. White light curves and pixel-level light curves were generated from the time series of 1D stellar spectra for both detectors.

We independently fitted white and spectral light curves from each detector using the `juliet` Python package (N. Espinoza et al. 2019), employing nested sampling via `dynesty` (J. S. Speagle 2020). We restricted the time series observations to $+1.0$ hr from the start, as the transit begins in the first half-hour (see top panel Figure 1). The period ($P = 7.4507245$ days), eccentricity ($e = 0$), and argument of periastron ($\omega = 90$) are fixed based on values from O. D. S. Demangeon et al. (2021) and R. Luque & E. Palle (2022). We fitted the planet-to-star radius ratio, mid-transit time, impact parameter, and semimajor axis ratio, including limb-darkening coefficients determined with a square-root law and a uniform prior. Additionally, we included a mean-out-of-transit offset ($mflux$) and a jitter parameter (σ_{w}) for white noise. To account for correlated noise, we used Gaussian processes (GP) using the `george` package with a Matérn 3/2 kernel (S. Ambikasaran et al. 2015; D. Foreman-Mackey et al. 2017). This method captures complex systematics and has been validated in ERS WASP-39b studies (A. D. Feinstein et al. 2023; L. Alderson et al. 2023). A log-uniform prior was set for the GP amplitude between 0.001 and 1000 ppm, and an exponential prior was set for the GP length scale, using time and the full-width half maximum (FWHM) as GP regressors. The white light-curve fitting results are shown in Figure 1, and the detailed best-fit parameters and confidence intervals are provided in Appendix Table 2. We determined the optimal systematics detrending model based on Bayesian log evidence, finding that the GP model with both time and FWHM as regressors offers the best fit. We evaluated several detrending approaches, including linear models with time and FWHM, and a GP with time only using the Matérn 3/2 kernel via the `celerite` package (D. Foreman-Mackey et al. 2017). For NRS1, the log-evidence values were 6700 for the transit-only model, 6778 for the linear time model, 6780 for the linear time plus FWHM model, 6782 for the GP with time only, and 6784 for the GP with both time and FWHM. Similarly, for NRS2, the GP model including both time and FWHM achieved the highest log-evidence value of 6405, compared to 6302 for the transit-only model, 6212 for the linear time model, 6219 for the linear time plus FWHM model, and 6282 for the GP with time only.

¹¹ <https://github.com/nespinoza/transitspectroscopy>

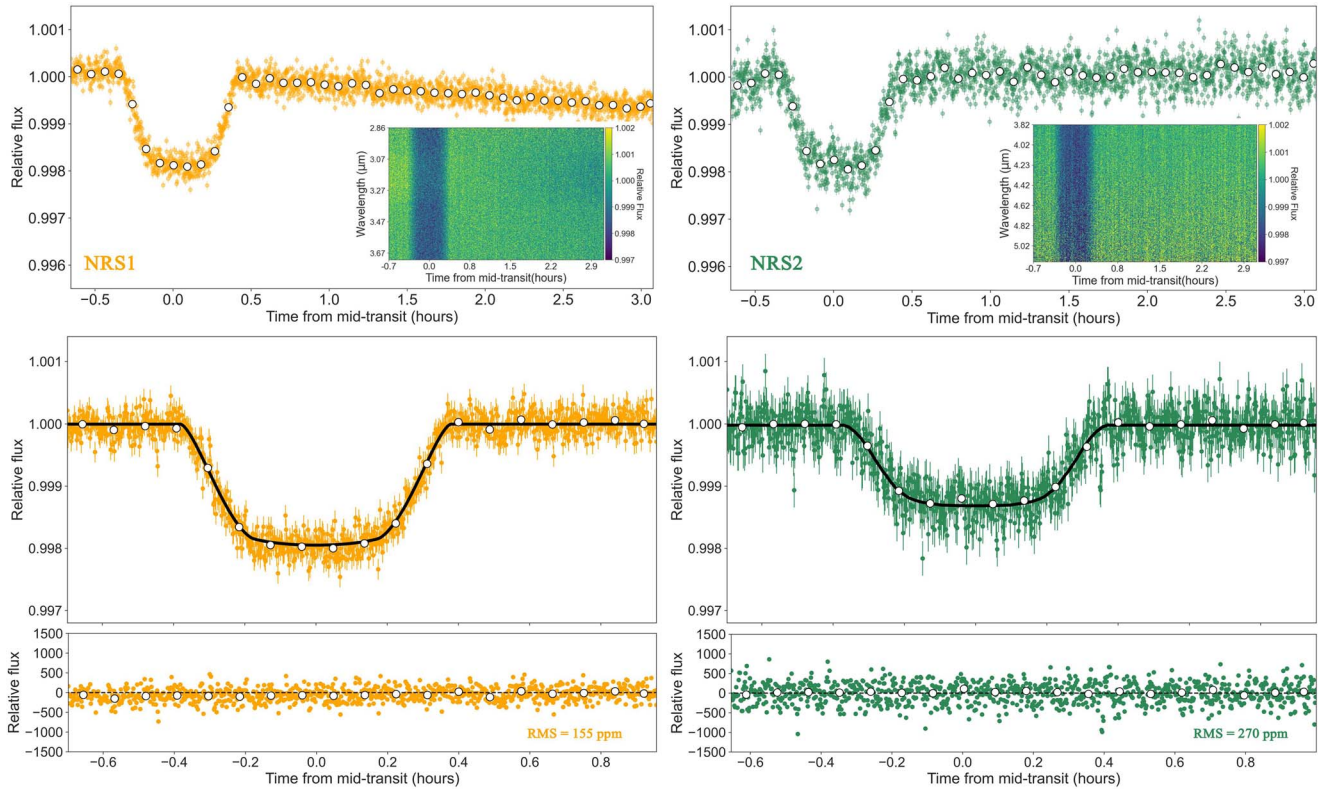


Figure 1. Top: raw white light curves for NRS1 (left) and NRS2 (right) from `transitspectroscopy` and spectral light-curve map. Middle: corrected white light curves (colored data points) overplotted with the best-fit transit model (black line) from `juliet`. Bottom: residuals between raw light curves and transit model. (The data used to create this figure are available in the [online article](#).)

For the spectral light curves, we used a similar setup but fixed the mid-transit time, impact parameter, and semimajor axis ratio based on the best-fit results from the white light curves. The fitted values are T_0 (BJD_{TDB}) = 2460121.112518755 $\pm 7 \times 10^{-5}$, $b = 0.925 \pm 0.004$, and $a/R_\star = 37.11 \pm 0.55$. Limb-darkening coefficients were determined using a truncated normal distribution centered on values estimated by the `exotic` (D. Grant & H. R. Wakeford 2022) package and PHOENIX models (T.-O. Husser et al. 2013). Given the high impact parameter, constraining these coefficients was challenging, as discussed in Figures B1 and B2. The transmission spectrum was obtained by binning pixel-level transit depths to a resolution of $R \sim 100$, resulting in 56 data points. Uncertainties in the final spectrum were calculated by determining the weighted mean and variance for each bin, with errors derived from the weighted contributions of the high-resolution spectra's errors and their associated variance. This spectrum can be found in Table 3.

3.2. Data Reduction with FIREFLY

We reduced the L98-59 d data using the Fast InfraRed Exoplanet Fitting Lyghtcurve (FIREFLY; Z. Rustamkulov et al. 2022, 2023) reduction suite. FIREFLY starts with a customized reduction using the STScI pipeline and the uncalibrated images and includes 1/f destriping at the group level before the ramp is fit. We applied a custom superbias step, where the STScI pipeline superbias was scaled separately for NRS1 and NRS2 to match the trace-masked count level median value of each integration. This procedure was introduced in S. E. Moran et al. (2023) to help reduce offsets between the

NRS1 and NRS2 detectors. The jump-step and dark-current stages of the STScI pipeline are skipped. We then use the custom-run 2D images after the gain scale step and perform customized cleaning of bad pixels, cosmic rays, and hot pixels.

We fit the transit light curves using a quadratic limb-darkening model (q_1 and q_2 ; D. M. Kipping 2013), along with a polynomial function of time to remove overall baseline trends. In addition, we tested detrending the lightcurves with the X- and Y-positions on the detector and the scaling factor used in the superbias step. We found the NRS1 detector to have a step trend that evolved over the first 0.04 days requiring a polynomial in time with orders 1, 2, 5, and 6. The higher-order trends modeled the trends seen at the beginning of the observation well. Conversely, NRS2 only required a second-order polynomial though a trend in Y-position was found to be needed. In addition, a trend for both NRS1 and NRS2 with the superbias scaling factor was found to be needed. We first fit for both q_1 and q_2 , but found q_2 to be weakly constrained and consistent with 0, so q_2 was fixed to zero throughout the rest of the analysis. a/R_\star , T_0 , and the impact parameter b were fit for both NRS1 and NRS2, then fixed to the weighted-average value of both detectors. The spectroscopic fits followed the same procedure. However, q_1 was found not to have a strong wavelength dependence when fit spectroscopically and was weakly constrained, so it was fixed to the weighted-average value for all wavelength channels ($q_1 = 0.117 \pm 0.017$). The light curves were binned to produce final transmission spectra with a resolution near $R=60$ with a total of 38 points.

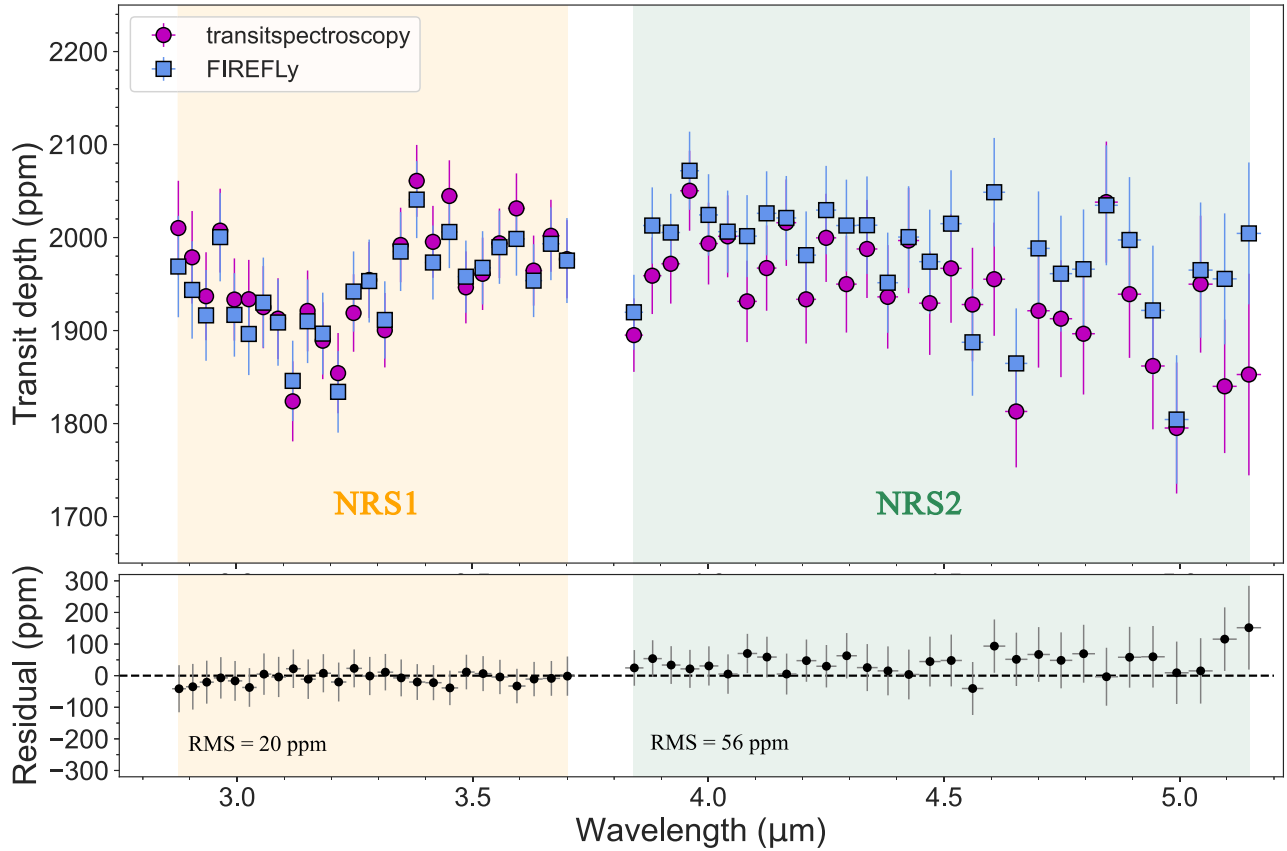


Figure 2. Transmission spectra of L98-59 d obtained using `transitspectroscopy` (pink) and `FIREFLY` (blue) pipelines. The spectral light curves from the two independent reductions were fitted using `juliet` with a similar parameterization at pixel resolution and then binned to $R \sim 100$. The residuals between the two reductions show a global offset between the two reductions for the NRS2 detector.

(The data used to create this figure are available in the [online article](#).)

3.3. Data Reductions Comparison

We fit the pixel-light curves from `transitspectroscopy` and `FIREFLY` reductions with the parameterization described in Section 3.1. The results are in Figure 2. While both spectra exhibit similar shapes, a systematic offset is observed for NRS2 detector transit depths between the two reductions, with `FIREFLY`'s transmission spectrum exhibiting higher transit depth values than `transitspectroscopy`. Specifically, there is a higher median of residuals for NRS2 (+46 ppm) compared to NRS1 (-8 ppm), potentially attributable to a different background treatment for the NRS2 detector. The rms of the residuals is found to be 56 ppm for NRS2 and 20 ppm for NRS1. Similarly, the light-curve fitting setup described in Section 3.2 is applied to `transitspectroscopy`'s light curves (see Figure B2).

4. Interpretation

We interpret the results using forward and retrieval modeling focusing on the transmission spectrum obtained with `transitspectroscopy` at $R \sim 100$.

4.1. Evidence of an Atmosphere from 1D Forward Modeling

We used `Exo-REM` (J.-L. Baudino et al. 2015; B. Charnay et al. 2018; D. Blain et al. 2021) to create a grid of transmission spectra for L98-59 d. `Exo-REM` is a 1D self-consistent radiative-convective code for exoplanets and brown dwarfs'

atmospheres. The atmosphere is modeled using 80 layers between 10^{-3} and 10^7 Pa, with an eddy diffusion coefficient of 10^{-8} $\text{cm}^2 \text{s}^{-1}$. We simulated a $300 \times$ solar atmosphere, including 13 absorbing species in a hydrogen-rich atmosphere, considering both equilibrium and out-of-equilibrium chemistry. The metallicity is the factor by which all the elemental abundances except H are multiplied compared to their solar abundances (K. Lodders 2010). For out-of-equilibrium chemistry, `Exo-REM` incorporates disequilibrium processes for $\text{CH}_4\text{-CO}$, $\text{CO}\text{-CO}_2$, and $\text{N}_2\text{-NH}_3\text{-HCN}$ reactions based on K. J. Zahnle & M. S. Marley (2014). The quenching level is determined by comparing the reaction timescale to the mixing time H^2/K_{zz} , where H is the atmospheric scale height and K_{zz} is the eddy diffusion coefficient. The abundance of the species is governed by the thermochemical equilibrium below the quenching level, where the temperature and pressure are high enough so that the kinetics dominate. The internal temperature was set to 70 K, controlling the position of the convective layer. We also tested a pure H_2O , CH_4 , CO_2 , and H_2S atmosphere.

Figure 3 shows the transmission spectrum obtained with `transitspectroscopy` and grid models from `Exo-REM`, along with corresponding χ^2 statistics. The pure H_2S model provides the best fit to the spectrum with a chi-square difference of around 19 with the flat line. This represents a statistically significant improvement in fit, exceeding 3σ (degrees of freedom = 56). However, the observed variations in the transmission spectrum for a pure H_2S model, which show differences of approximately 40 ppm, exceed the simple scale

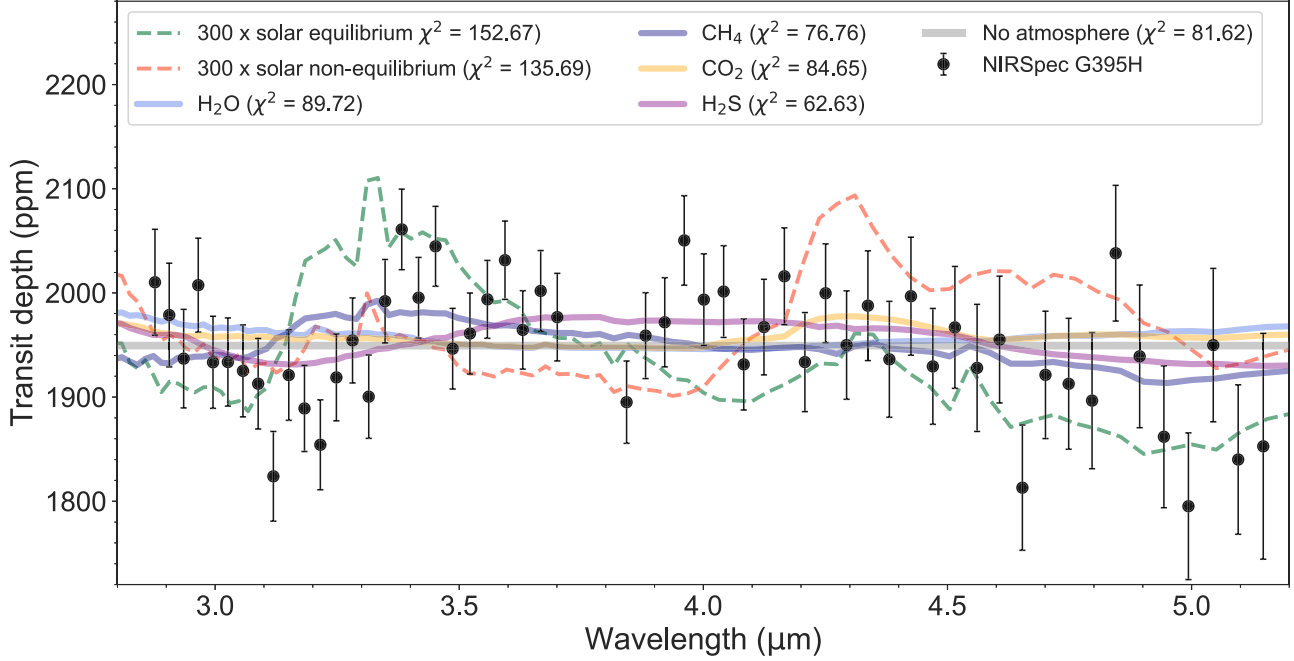


Figure 3. Transmission spectrum of L98-59 d obtained using `transitspectroscopy` and binned to $R \sim 100$ (black points) compared to forward models from Exo-REM (colored dashed and filled lines). The pure H₂S model provides the best fit according to χ^2 statistics. No offset is added between NRS1 and NRS2.

height prediction of ~ 5 ppm. This is estimated using a 416 K equilibrium temperature and 34 g cm^{-3} mean molecular weight. This discrepancy may arise from several factors including the modeling of the atmosphere with ExoREM, which simulates a pure H₂S atmosphere within a hydrogen-dominated framework, potentially resulting in an inflated effective scale height. Additionally, the use of cross section opacities made for hydrogen-dominated atmospheres and detailed atmospheric physics in our models may explain the larger signal compared to the simplified scale height calculation. Further investigation into the support for sulfur-bearing species opacities in the atmospheric model will be conducted using a Bayesian framework in Section 4.2. Cloud-free models with 300 times solar abundance exhibit large CH₄ features at $3.3 \mu\text{m}$ and CO/CO₂ features around $4.5 \mu\text{m}$, which are not observed in the L98-59 d transmission spectrum. Despite the pure H₂S model being a likely nonphysical atmospheric model, it is the best fit according to χ^2 statistics. The modeled flat line presented in Figure 3 is computed using the results of the retrieval analysis with TauREx for consistency (see Section 4.2). Using a weighted mean of spectrum points yields a chi-squared of 80.47, instead of 81.62. These results might indicate an atmosphere with the presence of sulfur-bearing species or stellar contamination.

4.2. Atmospheric and Stellar Contamination Retrieval Analyses

4.2.1. Retrieval Configurations

We conduct atmospheric and stellar contamination retrievals of L98-59 d's properties based on its observed spectra obtained through `transitspectroscopy` using TauREx 3 (A. F. Al-Refaie et al. 2021)¹² and exoretrievals (N. Espinoza et al. 2019).

For the atmospheric retrieval analysis, we used the Multinest algorithm (F. Feroz et al. 2009; J. Buchner et al. 2014) with 100 layers in the atmosphere, spanning from 10^{-3} to 10^6 Pa . The model included an evidence tolerance of 0.5 and 1500 live points. Stellar parameters were fixed (radius: $0.303 R_\odot$, T_{star} : 3415 K, and metallicity: -0.46). The planetary radius was fitted within the range of 0.79 – $2.37 R_\oplus$ to explore the full parameter space, account for uncertainties including limb-darkening effects, and ensure robustness in the model. The temperature-pressure profile ranged from 200 to 600 K. Clouds were modeled as gray clouds with a top pressure between 10^{-3} and 10^6 Pa . The helium-to-hydrogen ratio was set to 0.17, and an offset between NRS1 and NRS2 transmission spectra was fitted uniformly between -100 and $+100 \text{ ppm}$ using the `taurex-offset` plugin.¹³

Equilibrium chemistry: We used `ggchem`¹⁴ (P. Woitke et al. 2018) for equilibrium chemistry, including molecular line lists and continuum from the ExoMol project (J. Tennyson et al. 2016; K. L. Chubb et al. 2021), HITEMP (J. Tennyson & S. N. Yurchenko 2018), and HITRAN (L. S. Rothman et al. 1987, 2010). The active molecules included are: H₂O (O. L. Polyansky et al. 2018), CO (G. Li et al. 2015), CO₂ (L. S. Rothman et al. 2010), CH₄ (S. N. Yurchenko et al. 2017), NH₃ (S. N. Yurchenko et al. 2011), H₂S (A. A. A. Azzam et al. 2016), HCN (R. J. Barber et al. 2014), C₂H₂ (K. L. Chubb et al. 2020), C₂H₄ (B. P. Mant et al. 2018), SiO (S. N. Yurchenko et al. 2021), SO₂ (D. S. Underwood et al. 2016), TiO (L. K. McKemmish et al. 2019), and VO (L. K. McKemmish et al. 2016). Collision-induced absorption (CIA) and Rayleigh scattering were also considered. We fitted for C/O and S/O ratios (0.1–2) and atmospheric metallicity (1–1000 times solar).

Free chemistry: The active molecules included are H₂O, CO, CO₂, CH₄, SiO, H₂S, HCN, NH₃, and SO₂. CIA and Rayleigh

¹² https://github.com/ucl-exoplanets/TauREx3_public

¹³ <https://github.com/QuentChangeat/taurex-offset>

¹⁴ <https://pypi.org/project/taurex-ggchem/>

Table 1
Summary of Atmospheric Retrieval Results Using TauREx on L98-59 d Transmission Spectrum Obtained with `transitspectroscopy`'s Reduction at $R \sim 100$

Parameters	Equilibrium		Free Chemistry		Free—with N ₂		Free—H ₂ S and SO ₂ only	
	Prior	Posterior	Prior	Posterior	Prior	Posterior	Prior	Posterior
R_p , ref (R _⊕)	$\mathcal{U}(0.79, 2.37)$	$1.45^{+0.01}_{-0.01}$	$\mathcal{U}(0.79, 2.37)$	$1.43^{+0.01}_{-0.01}$	$\mathcal{U}(0.79, 2.37)$	$1.43^{+0.01}_{-0.01}$	$\mathcal{U}(0.79, 2.37)$	$1.43^{+0.01}_{-0.01}$
T_p (K)	$\mathcal{U}(200, 600)$	490^{+74}_{-134}	$\mathcal{U}(200, 600)$	426^{+111}_{-105}	$\mathcal{U}(200, 600)$	521^{+54}_{-86}	fixed	416
log(P_{clouds}) (Pa)	$\mathcal{U}(-3, 6)$	$4.18^{+1.16}_{-1.67}$	$\mathcal{U}(-3, 6)$	$5.16^{+0.54}_{-0.75}$	$\mathcal{U}(-3, 6)$	$5.17^{+0.52}_{-0.61}$	$\mathcal{U}(-3, 6)$	$5.27^{+0.50}_{-0.61}$
mmw (amu)	...	$32.13^{+1.50}_{-8.31}$...	$9.18^{+2.51}_{-2.41}$...	$13.71^{+4.04}_{-3.46}$...	$9.30^{+2.46}_{-1.59}$
Offset (ppm)	$\mathcal{U}(-100, 100)$	$14.6^{+14.6}_{-14.1}$	$\mathcal{U}(-100, 100)$	$37.6^{+15.0}_{-16.4}$	$\mathcal{U}(-100, 100)$	$35.5^{+14.1}_{-16.0}$	$\mathcal{U}(-100, 100)$	$31.4^{+13.4}_{-13.6}$
Z	$\mathcal{U}(1, 1000)$	747^{+167}_{-239}
C/O	$\mathcal{U}(0.1, 2)$	$1.23^{+0.51}_{-0.58}$
S/O	$\mathcal{U}(0.1, 2)$	$1.54^{+0.32}_{-0.52}$
N ₂ /H ₂	$\mathcal{U}(0.001, 2)$	$0.64^{+0.62}_{-0.35}$
log(H ₂ O)	$\mathcal{U}(-12, 0.3)$	< -5.0	$\mathcal{U}(-12, 0.3)$	< -5.0
log(CO)	$\mathcal{U}(-12, 0.3)$	< -2.5	$\mathcal{U}(-12, 0.3)$	< -2.5
log(CO ₂)	...	—	$\mathcal{U}(-12, 0.3)$	< -2.5	$\mathcal{U}(-12, 0.3)$	< -2.5
log(CH ₄)	...	—	$\mathcal{U}(-12, 0.3)$	< -6.0	$\mathcal{U}(-12, 0.3)$	< -6.0
log(SiO)	$\mathcal{U}(-12, 0.3)$	< -2.0	$\mathcal{U}(-12, 0.3)$	< -1.0
log(H ₂ S)	$\mathcal{U}(-12, 0.3)$	$-0.74^{+0.14}_{-0.49}$	$\mathcal{U}(-12, 0.3)$	$-1.31^{+0.48}_{-2.35}$	$\mathcal{U}(-12, 1)$	$-0.66^{+0.13}_{-0.11}$
log(HCN)	$\mathcal{U}(-12, 0.3)$	< -5.0	$\mathcal{U}(-12, 0.3)$	< -5.0
log(NH ₃)	$\mathcal{U}(-12, 0.3)$	< -6.0	$\mathcal{U}(-12, 0.3)$	< -6.0
log(SO ₂)	$\mathcal{U}(-12, 0.3)$	$-5.64^{+4.41}_{-4.12}$	$\mathcal{U}(-12, 0.3)$	$-3.80^{+2.25}_{-4.91}$	$\mathcal{U}(-12, 1)$	< -2.0
Criteria	Flat line ^a	Model	Flat line	Model	Flat line	Model	Flat line	Model
χ^2	83.05	70.37	96.54	49.68	86.00	50.08	86.24	50.74
AIC	91.05	84.38	104.54	75.68	94.00	78.08	94.24	60.74
BIC	99.15	98.55	112.64	102.01	102.10	106.44	102.34	70.87
log \mathcal{Z}	458.00	460.31	451.18	464.99	456.43	464.92	456.36	468.53
Significance (σ)	...	2.7	...	5.6	...	4.5	...	5.3

Note.

^a The statistics on the flat-line model are computed for each spectrum with the fitted offset applied.

opacities were included. We fitted the abundance of each molecule ($\log(X_{\text{VMR}})$) between 10^{-12} and 0.3 (between -12 and -0.5 in log space), ensuring the total molecular abundances never exceed one.

Free chemistry with N₂: The setup is similar to the free chemistry retrieval but included N₂ as an inactive gas. The N₂/H₂ ratio was fitted between 0.001 and 2.

Flat line: The flat line is a retrieval with no opacity sources, fitting for planetary radius and temperature. This was used to assess the significance of the atmospheric detection using Bayesian evidence, evaluated using Bayes's theorem. The Bayes factor, positively designed, is computed between an atmospheric model and the flat line and then converted in σ significance using the formalism of R. Trotta (2008) and B. Benneke & S. Seager (2013). This retrieval is performed for each atmospheric retrieval on the transmission spectrum with the retrieved offset applied and fixed.

4.2.2. Retrieval Results: An Atmosphere around L98-59d?

The retrieval results using `transitspectroscopy` reduction are summarized in Table 1. We detected an atmosphere around L98-59 d at 5.6σ with the free chemistry retrieval and at 2.7σ with the equilibrium chemistry retrieval. Both retrievals report a high abundance of H₂S: $\log(\text{H}_2\text{S}) = -0.74^{+0.14}_{-0.49}$ (free chemistry) and $\log(\text{H}_2\text{S}) = -0.21^{+0.07}_{-0.09}$ (equilibrium), with Bayesian evidences $\log \mathcal{Z} = 464.99$ and

$\log \mathcal{Z} = 460.31$, respectively. The flat-line fits yield $\log \mathcal{Z} = 451.19$ and $\log \mathcal{Z} = 458.00$.

The free chemistry retrieval best-fit model is presented in Figure 4 and the corresponding posterior distributions are in Figure C1, while the equilibrium chemistry retrieval is presented in Figures C2 and C3. The results align with A. Banerjee et al. (2024), hereafter Paper II, using NEMESISPY (P. G. J. Irwin et al. 2008; J. Yang et al. 2023). An offset of $37.6^{+15.0}_{-16.4}$ ppm was found between NRS2 and NRS1 with transit depths higher for NRS2. Both models suggest significant H₂S opacity, with CO₂ (equilibrium) and SO₂ (free chemistry) as additional opacity contributors. The free chemistry model fits significantly better than the equilibrium model by 3.8σ suggesting that L98-59 d's atmosphere is not at equilibrium. The SO₂ volume mixing ratio (VMR) in the free retrieval shows a bimodal distribution, with a constraint either above -1.0 or an upper limit below -1.5 . However, we can put upper limits on every other molecule of the fit. In particular, H₂O's VMR is constrained below 10^{-5} suggesting a water-poor atmosphere for this planet that has density compatible with a water-rich composition (R. Luque & E. Palle 2022). Excluding both H₂S and SO₂ from the free chemistry retrieval indicates that the model with these molecules is favored at 4.5σ using model comparison with the Bayes factor.

Adding N₂ as an inactive gas in the free chemistry retrieval did not significantly alter results, favoring the atmospheric model over a flat line at 4.5σ . The only strongly constrained parameters are the planetary radius at 10 bars,

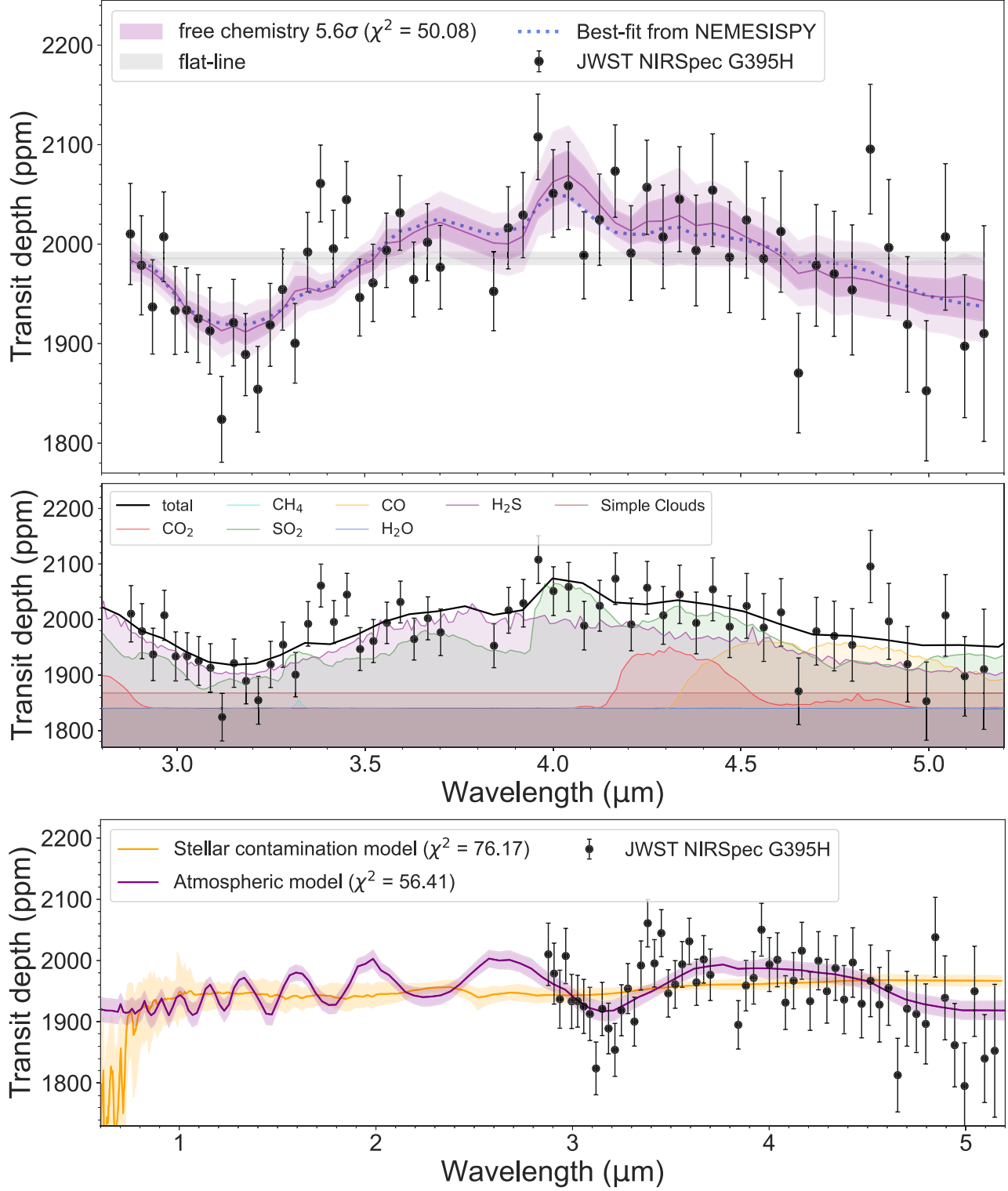


Figure 4. Top panel: transmission spectrum of L98-59 d obtained using `transitspectroscopy` and binned to $R \sim 100$ (black points) compared to a free chemistry retrieval model from `TauREx` (purple) and `NEMESISPY` (dashed blue) from Paper II. Middle: opacity contributions from the best-fit model. The model suggests a contribution from H₂S (purple) and SO₂ (green) opacities. Bottom: transmission spectrum compared to stellar (yellow) and atmospheric (purple) retrieval models.

(The data used to create this figure are available in the [online article](#).)

the log VMR of H₂S, toward the edge of the prior (0.3), and the top pressure of the gray clouds. The log VMR of SO₂ is tentatively constrained. For this reason, we run a fit with H₂S and SO₂ as the only active molecular opacity sources,

increasing the prior range to 1, and fit for their molecular abundances while fixing the temperature to the equilibrium temperature at 416 K. This atmospheric model is preferred at 5.3σ to a flat line.

4.2.3. Stellar Contamination: Is There an Atmosphere or Stellar Inhomogeneities?

One of the early results from observations of small planets with JWST is how important it is to consider heterogeneities on the surface of the host star when looking for atmospheric signals in transmission. Multiple small planet observations have shown contamination from the presence of hot and cold spots on the photosphere of the host star during transit, which imprint false slopes and can potentially even inject false molecular features into the transmission spectrum (see, e.g., O. Lim et al. 2023; S. E. Moran et al. 2023). This is especially important for planets orbiting small M stars like L98-59, which are known to show a high level of magnetic activity and associated surface features (B. V. Rackham et al. 2018).

To test if the spectrum could be explained by stellar contamination caused by inhomogeneities (hot and/or cold spots) on the stellar surface, we carry out retrievals using exoretrievals (N. Espinoza et al. 2019). Based on the framework presented in B. V. Rackham et al. (2018), this allows us to model the spectrum created by occulted and/or unocculted spots on the stellar surface during the transit, by replacing a portion of the surface with a stellar model of another temperature. Since we do not see any evidence of spot crossing events in the light curves, we only consider unocculted spots in our retrieval. We consider the cases of only hot spots, only cold spots, or both being present on the stellar surface, and allow these spot temperatures to vary over a large parameter space, from 1800 to 3250 K and from 3550 to 5000 K, respectively, for a photospheric temperature of 3415 ± 135 . We also place a wide prior on the spot covering fraction, allowing the spots to together cover up to the entirety of the unocculted photosphere. We also tested using both default PHOENIX models and BT-SETTL models considering the relatively low photospheric temperature of L98-59, but saw no appreciable difference in the results. Even with this very large explored parameter space, none of the stellar contamination models are able to explain the features seen in the spectrum, especially those at the longest wavelengths. Figure 4 (bottom panel) shows the best-fit model from the stellar contamination retrieval results. The corresponding posterior distributions are in Figure C4. We also show the best-fit model from an atmospheric retrieval analysis with TauREx. In these fits, no offset between NRS1 and NRS2 is applied. The $\text{H}_2\text{S}/\text{SO}_2$ -rich atmosphere is favored compared to the stellar contamination, suggesting the large feature between 3.3 and 4.8 μm , if confirmed by follow-up observations, and originates from the atmosphere.

4.2.4. Comparison between Data Reductions

To confirm the atmospheric detection, we applied the free chemistry retrieval setup to the FIREFLy transmission spectrum at $R \sim 100$ and to the spectrum obtained at $R \sim 60$ from an independent fitting method (see Figure 2). The results of these fits are shown in Figure C5. The atmospheric detection was less significant with FIREFLy, yielding 3.0σ for $R \sim 100$ and 2.6σ for $R \sim 60$ spectra.

The discrepancy at $R \sim 100$ primarily arises from differences at longer wavelengths in the NRS2 detectors. transit-spectroscopy data showed a decrease in transit depth between 4.5 and 5 μm , fitted with H_2S opacity (see the middle panel in Figure 4) while FIREFLy's transmission spectrum remains flat across the entire wavelength range of the NRS2

detector. However, sulfur-bearing species consistently appeared as the primary source of opacity in all retrievals. The NRS1 and NRS2 offset varied by reduction method: +37 ppm for transitspectroscopy and -14 ppm for FIREFLy, both consistent with zero at 1σ . Removing this offset is unlikely to significantly change the FIREFLy result given the small offset within 1σ uncertainty.

The $R \sim 60$ spectrum from FIREFLy with an independent light-curve fitting showed a tentative atmospheric detection (2.6σ). This finding raises concerns, suggesting that the detection made with other binning and light-curve fitting may be attributed to random noise. Specifically, the discrepancy observed at shorter wavelengths, between 3 and 3.3 μm , between the two reductions could account for this result (see Figure B2). The variability observed in FIREFLy's transmission spectrum in this wavelength range resulted in a seemingly flatter spectrum and a statistically nondetection, whereas transitspectroscopy's data indicated a pronounced decrease in transit depths, well-fitted by H_2S 's opacity (see the middle panel in Figure 4). We note that by employing the same light-curve fitting and binning, the decrease is observed in FIREFLy's reduction as well (see Figure 2).

In Appendix C, we assess the impact of introducing an offset between NRS1 and NRS2 transit depths on atmospheric detection for L98-59 d (see Figure C5) and evaluate the influence of spectral resolution (see Appendix C.6).

5. Conclusions

We presented one transit observation of the Super-Earth L98-59 d with the JWST NIRSpec G395H mode. Our study highlights several challenges encountered in the data reduction process when analyzing transmission spectra of small planets. First, the limb-darkening coefficients pose a challenge for grazing planets due to their impact on the light-curve fitting process. Even though our two data reductions agree when using the same limb-darkening coefficients, remaining discrepancies at specific wavelengths led to different interpretations in the retrieval analysis.

From this single transit, our analysis suggests no stellar contamination, but hints at potential atmospheric detection, though significance varies with data reduction methods. In the best-case scenario, we detected an atmosphere with a 5.6σ significance. An independent analysis led to a 2.6σ tentative detection. Atmospheric retrieval models suggest the presence of sulfur-bearing species with hydrogen and helium as background gases, although the inferred high abundance levels are not yet well understood. The discovery of sulfur dioxide in the atmospheres of hot Jupiters (L. Alderson et al. 2023; Z. Rustamkulov et al. 2023; D. Powell et al. 2024) and Neptune-like planets (A. Dyrek et al. 2024; B. Benneke et al. 2024; M. Holmberg & N. Madhusudhan 2024) are key results in early JWST analysis being evidence of photochemistry. Sulfur species and clouds are expected in giant planets and brown-dwarf atmospheres (C. V. Morley et al. 2012; J. Polman et al. 2023; S.-M. Tsai et al. 2023). I. J. M. Crossfield (2023) showed that the ability to detect SO_2 in exoplanet atmospheres provides a crucial test for different planet formation models, revealing that sulfur's volatility and abundance can distinguish between planetesimal and pebble-accretion scenarios. Photochemistry could also produce H_2S and SO_2 in terrestrial atmospheres, as predicted by R. Hu et al. (2013). The presence of sulfur-bearing species in rocky planets could also be

explained by out-gassing, volcanism, and interaction between the atmosphere and the rocky surface. The recent study of L. J. Janssen et al. (2023) investigated sulfur's presence and detectability in rocky exoplanet atmospheres using thermochemical equilibrium models at the crust–atmosphere interface, considering surface temperatures of 500–5000 K and pressures of 1–100 bar, with various element abundances based on common rock compositions. They showed that at temperatures between 1000 and 2000 K, gaseous sulfur concentrations can reach up to 25%. They conclude that the most abundant sulfur molecules are SO , SO_2 , H_2S , and S_2 with potentially detectable features in transmission spectra around 4, 7–8, and beyond $15\ \mu\text{m}$.

The difference between the data reductions and the uncertainties on the data points is magnified when dealing with observations from a single visit. (E. M. May et al. 2023), highlighting for GJ 1132b the importance of multiple visits when claiming atmospheric detection for rocky planets. Our transmission spectrum might have random noise fluctuations, which suggested the detection of an atmosphere that emphasizes the need for multiple transits observations. This result will have to be compared to the second G395H visit from Cycle 2 GO program 4098 (PI: Benneke) but also to the NIRISS SOSS transit from Cycle 1 GTO program 1201 (PI: Lafrenière).

Only hints of atmospheric detections have been found so far for rocky planets with radii below $1.6\ R_{\oplus}$ around M dwarfs. Notably, planets from the GO program 1981 (PIs: Stevenson and Lustig-Yaeger), in order of increasing radius, include GJ 341 b with a radius of $0.92\ R_{\oplus}$ (J. Kirk et al. 2024), LHS 475 b with $0.99\ R_{\oplus}$ (J. Lustig-Yaeger et al. 2023), GJ 1132b with $1.1\ R_{\oplus}$ (E. M. May et al. 2023), and GJ 486 b with $1.3\ R_{\oplus}$ (S. E. Moran et al. 2023), yet they have not provided compelling evidence of an atmosphere. However, similar JWST observations on planets with radii above $1.6R_{\oplus}$, such as K2-18 b ($2.61\ R_{\oplus}$; N. Madhusudhan et al. 2023), TOI-270 d ($2.31\ R_{\oplus}$), and 55 Cancri e ($1.97\ R_{\oplus}$; R. Hu et al. 2024) have provided strong molecular detections. If confirmed, the detection of sulfur-bearing species in a hydrogen-dominated atmosphere around L98-59 d, a planet with a radius of $1.58\ R_{\oplus}$

Earth radii, would be a significant result, as it lies right at the cutoff predicted by L. A. Rogers (2015) and J. G. Rogers et al. (2021) for planets to have retained their primary hydrogen–helium atmosphere. Planets with a radius above $1.6R_{\oplus}$ have a density too low to be compatible with a silicate and iron-only core composition. A second study Paper II, from the NIRSpec GTO collaboration will explore in more detail the possible atmospheric scenarios for L98-59 d.

Acknowledgments

N.H.A. acknowledges support by the National Science Foundation Graduate Research Fellowship under grant No. DGE1746891.

The JWST data presented in this Letter were obtained from the Mikulski Archive for Space Telescopes (MAST) at the Space Telescope Science Institute. The specific observations analyzed can be accessed via [10.17909/nrxs-cx46](https://doi.org/10.17909/nrxs-cx46).

Facility: JWST (NIRSPEC G395H).

Appendix A Data Reduction: Light-curve Best-fit Results

This appendix presents the best-fit results for the white light curves using transit spectroscopy's reduction, summarized in Table 2, and Table 3 presents the extracted transit depth from the spectral light-curve fit at R100. We fitted the white and spectral light curves from each detector using the juliet Python package with nested sampling via dynesty. The observations were restricted to ± 1.0 hours from the start of the transit, with fixed period, eccentricity, and argument of periastron values from prior studies. The fit included parameters such as the planet-to-star radius ratio and impact parameter, with correlated noise handled by Gaussian Processes using a Matérn 3/2 kernel. The white light-curve results are shown in Figure 1, with detailed parameters and confidence intervals in Table 2. The optimal detrending model, determined by Bayesian log evidence, was the GP model with time and FWHM as regressors.

Table 2
L98-59 d White Light-curve Fitting Results for the `transitspectroscopy` Reduction Using `juliet`

Parameter	Prior	NRS1			NRS2		
		Median	68% CI Upper	68% CI Lower	Median	68% CI Upper	68% CI Lower
T_0 (BJD _{TDB})	$\mathcal{N}(2460121.1107, 0.2)$	2,460,121.1125	+0.000076	-0.000073	2,460,121.1125	+0.000162	-0.000168
a/R_{\star}	$\mathcal{N}(37.1, 0.5)$	37.098	+0.449	-0.450	37.117	+0.101	-0.100
b	$\mathcal{N}(0.92, 0.5)$	0.9230	+0.0032	-0.0034	0.9291	+0.0078	-0.0079
$q1$	$\mathcal{U}(0.0, 1.0)$	0.3722	+0.274	-0.162	0.4672	+0.347	-0.315
$q2$	$\mathcal{U}(0.0, 1.0)$	0.6287	+0.259	-0.356	0.5869	+0.284	-0.369
R_p/R_{\star}	$\mathcal{U}(0.0, 0.2)$	0.0468	+0.0012	-0.0010	0.0385	+0.0098	-0.0110
$mflux$	$\mathcal{N}(0.0, 0.1)$	-0.000025	+0.000117	-0.000120	0.000178	+0.000477	-0.000432
σ_{w}	$\log \mathcal{U}(10^{-5}, 1000.0)$	142.50	+4.48	-4.44	258.14	+8.11	-7.52
σ_{GP}	$\log \mathcal{U}(0.001, 1000.0)$	106.45	+64.35	-31.47	655.99	+205.82	-182.66
GP _{malpha0}	Exp(1.0)	0.305	+0.441	-0.207	3.751	+2.073	-1.396
GP _{malpha1}	Exp(1.0)	0.0202	+0.0224	-0.0124	0.0025	+0.0030	-0.0013

Note. Description of parameters: mid-transit time (BJD_{TDB}). Ratio of the semimajor axis to the stellar radius. Planet to star radius ratio. First limb-darkening coefficient of the square-root law with the D. M. Kipping (2013) parameterization. Second limb-darkening coefficient. Out-of-transit flux offset. White noise jitter parameter. GP amplitude. GP length scales.

Table 3
L98-59 d Extracted Transit Depths from `transitspectroscopy`
at $R \sim 100$

Wavelength (μm)	Transit Depth	Transit Depth Error	Bin Size (μm)
2.8768	0.002010	0.000051	0.01460
2.9060	0.001979	0.000050	0.01460
2.9356	0.001937	0.000047	0.01495
2.9654	0.002007	0.000045	0.01495
2.9956	0.001933	0.000044	0.01525
3.0261	0.001934	0.000042	0.01525
3.0570	0.001925	0.000044	0.01560
3.0881	0.001913	0.000043	0.01555
3.1193	0.001824	0.000043	0.01560
3.1509	0.001921	0.000043	0.01595
3.1830	0.001889	0.000041	0.01620
3.2483	0.001919	0.000042	0.01655
3.2814	0.001954	0.000041	0.01655
3.3146	0.001900	0.000040	0.01660
3.3481	0.001992	0.000040	0.01690
3.3822	0.002061	0.000039	0.01720
3.4166	0.001995	0.000039	0.01725
3.4514	0.002045	0.000038	0.01755
3.4865	0.001946	0.000039	0.01750
3.5219	0.001961	0.000039	0.01790
3.5576	0.001994	0.000037	0.01785
3.5937	0.002031	0.000038	0.01820
3.6301	0.001964	0.000038	0.01820
3.6668	0.002002	0.000039	0.01850
3.7008	0.001977	0.000042	0.01550
3.8428	0.001895	0.000040	0.01945
3.8817	0.001959	0.000041	0.01945
3.9209	0.001972	0.000043	0.01980
3.9608	0.002050	0.000043	0.02010
4.0010	0.001994	0.000044	0.02010
4.0415	0.002001	0.000044	0.02045
4.0827	0.001931	0.000044	0.02070
4.1242	0.001967	0.000046	0.02075
4.1659	0.002016	0.000046	0.02100
4.2080	0.001934	0.000048	0.02105
4.2504	0.001999	0.000047	0.02135
4.2934	0.001950	0.000052	0.02165
4.3370	0.001988	0.000053	0.02200

Table 3
(Continued)

Wavelength (μm)	Transit Depth	Transit Depth Error	Bin Size (μm)
4.3810	0.001936	0.000056	0.02195
4.4252	0.001997	0.000057	0.02230
4.4701	0.001929	0.000056	0.02255
4.5152	0.001967	0.000058	0.02260
4.5606	0.001928	0.000061	0.02285
4.6067	0.001955	0.000061	0.02320
4.6534	0.001813	0.000060	0.02350
4.7007	0.001921	0.000061	0.02380
4.7483	0.001913	0.000063	0.02375
4.7961	0.001897	0.000065	0.02410
4.8445	0.002038	0.000065	0.02435
4.8936	0.001939	0.000068	0.02470
4.9433	0.001862	0.000068	0.02495
4.9935	0.001795	0.000070	0.02530
5.0443	0.001950	0.000074	0.02555
5.0954	0.001840	0.000072	0.02550
5.1467	0.001853	0.000108	0.02585

(This table is available in machine-readable form in the [online article](#).)

Appendix B Data Reduction: Treatment of the Limb-darkening Coefficients

L98-59 d had a high impact parameter $b > 0.9$, which makes it challenging to constrain the limb-darkening coefficient in the light-curve fitting. The choice of the limb-darkening coefficient treatment impacts the extracted transit spectrum, particularly the absolute transit depth value. First, we ran tests: one involving fitting the limb-darkening coefficients uniformly between 0 and 1 using a quadratic law, and another using a square-root law. For this test, we fit the light curves from the `transitspectroscopy`'s reduction at pixel resolution and bin the spectrum after. The results of this test are in Figure B1. We note that there is a 400 ppm offset between the two resulting transit spectra. The fit involving the quadratic law has a higher mean transit depth and lower precision. The shape of the spectrum is the same, but the transit depth values and precision are sensitive to the choice of the limb-darkening treatment.

Additionally, we perform a fit with fixed limb-darkening coefficients ($q_1 = 0.13$ and $q_2 = 0.0$), derived from the combined best fit of NRS1 and NRS2 white light curves, with $q_2 = 0.0$ being unconstrained. This parameterization is applied to pixel-level `transitspectroscopy` light curves, while FIREFLy light curves are binned to an $R \sim 60$ and fitted with these fixed coefficients and an independent detrending linear model. This fitting is described in Section 3.2. The results of this additional test are in Figure B2.

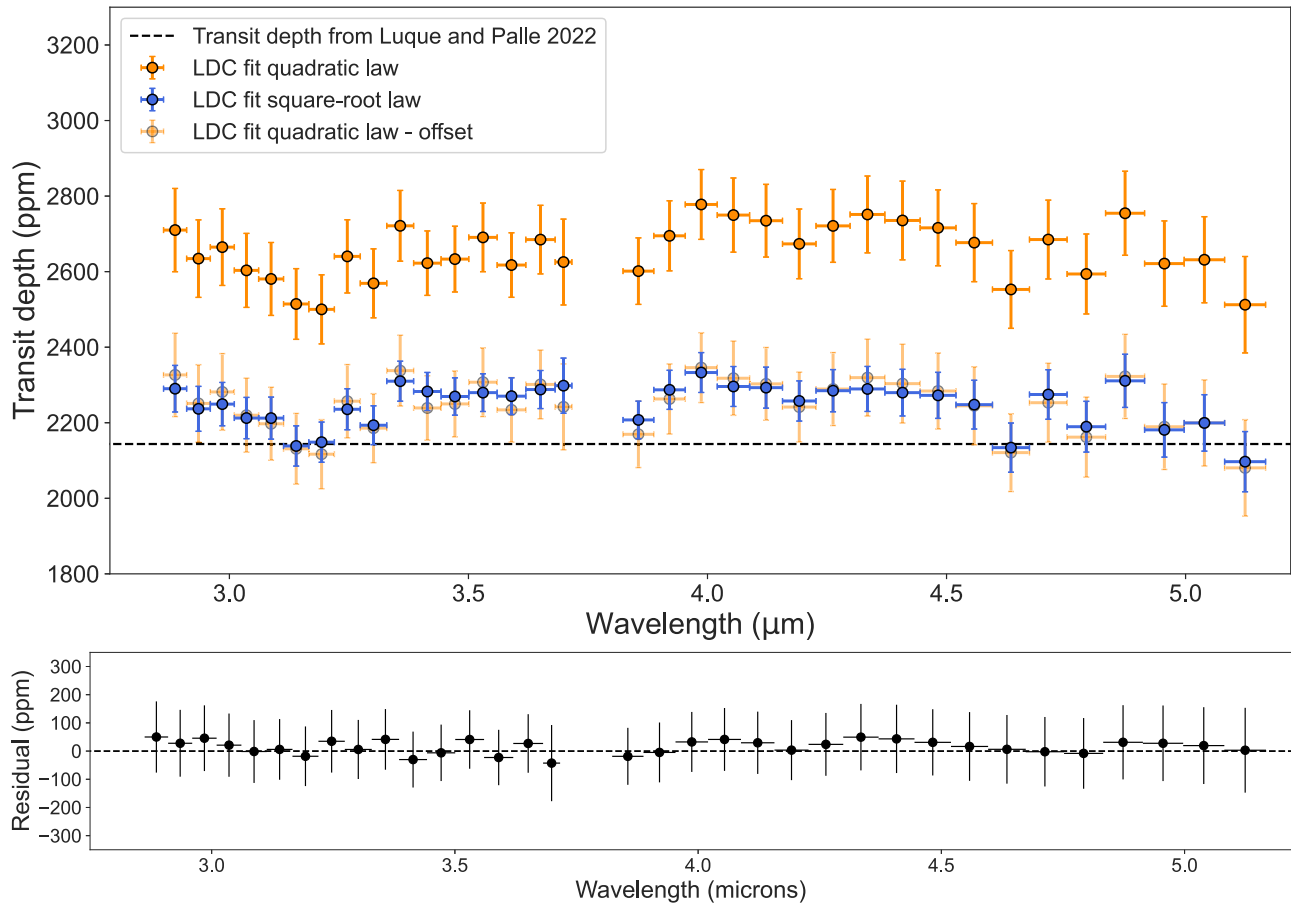


Figure B1. Top: transmission spectra of L98-59 d obtained using the reductions from `transitspectroscopy` and binned to a resolution of $R \sim 60$. The two spectra are derived by fitting the limb-darkening coefficients uniformly between 0 and 1 using a quadratic law (orange) and employing a square-root law (blue). The light orange points are obtained by applying an offset corresponding to the median differences between the two spectra. Bottom: residuals between the two transmission spectra after subtraction of the median transit depth. Each detector is treated independently. The shape of the two spectra is similar, but there is a 400 ppm offset between the two reductions.

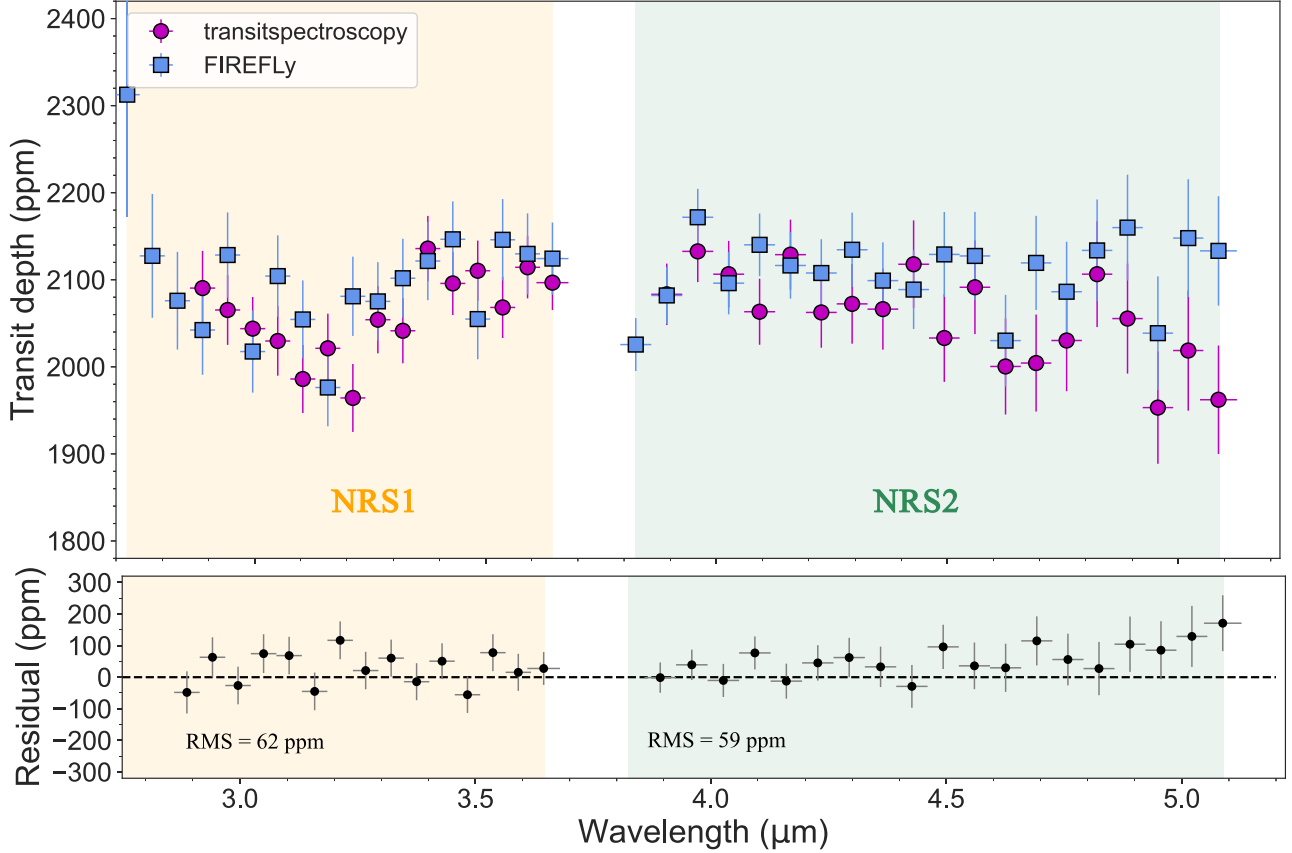


Figure B2. Transmission spectra of L98-59 d obtained using `transitspectroscopy` (pink) and `FIREFLY` (blue) pipelines. The spectral light curves from the two independent reductions were fitted independently. `transitspectroscopy` are fitted at pixel-level resolution using Gaussian processes to model the noise and then binned to the native resolution of the `FIREFLY`'s reduction to approximately an $R \sim 60$. `FIREFLY` light curves are binned to $R \sim 60$ and then fitted using a linear detrending model. For both fittings, the coefficients of the limb-darkening coefficients are fixed to $q_1 = 0.13$ and $q_2 = 0.0$. (The data used to create this figure are available in the [online article](#).)

Appendix C Additional Retrieval Analysis and Figures

This appendix presents the retrieval analysis results for the transmission spectrum of L98-59 d. We performed both atmospheric (see Appendices C1, C2, and C4) and stellar contamination (see Appendix C3) retrievals using TauREx 3 and exoretrievals. The atmospheric analysis incorporated equilibrium and free chemistry models. The equilibrium model included H₂O, CO, CO₂, CH₄, NH₃, and H₂S, accounting for CIA and Rayleigh scattering, while the free chemistry model expanded to include SiO, HCN, and SO₂, allowing for a wider range of abundances. A flat-line model was also used to assess

the significance of atmospheric detection through Bayesian evidence. For stellar contamination, we examined fixed stellar parameters and various planetary radii to ensure the robustness of the analysis. The results, including the posterior distributions for atmospheric (see Figures C1, C2, C3) and stellar contamination models (see Figure C4), are detailed below. Appendix Figure C5 shows the results of applying the free chemistry retrieval setup to the `FIREFLY` transmission spectrum at $R \sim 100$ and to an independently fitted spectrum at $R \sim 60$. The atmospheric detection was less significant with `FIREFLY`, with 3.0σ for $R \sim 100$ and 2.6σ for $R \sim 60$, suggesting remaining random noise at shorter wavelengths.

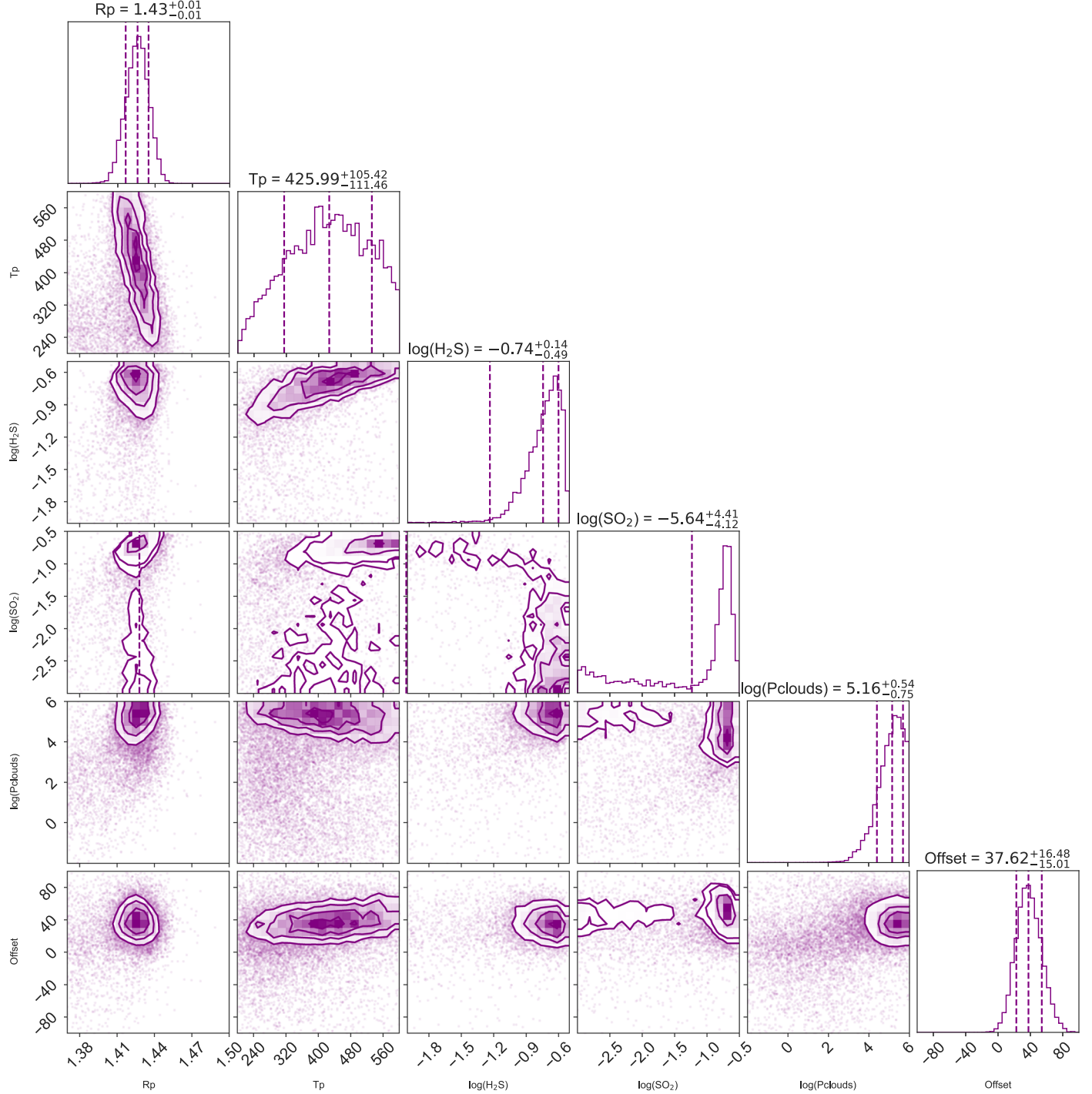


Figure C1. Posterior distributions from the free retrieval analysis. Not all parameters in the fit are plotted for clarity.

C.1. Free Chemistry Retrieval Analysis

We conducted a retrieval analysis using TauREx 3 with free chemistry on the transitspectroscopy reduction at R100. We present the posterior distributions from this free retrieval analysis in Figure C1. For clarity, not all parameters from the fit are plotted.

C.2. Equilibrium Chemistry Retrieval Analysis

We conducted a retrieval analysis using TauREx 3 with equilibrium chemistry, employing the ggchem plugin, on the transitspectroscopy reduction at R100. Here, we present the best-fit atmospheric model to the extracted transit depths (see Figure C2), including opacity contributions from the best-fit model. The model

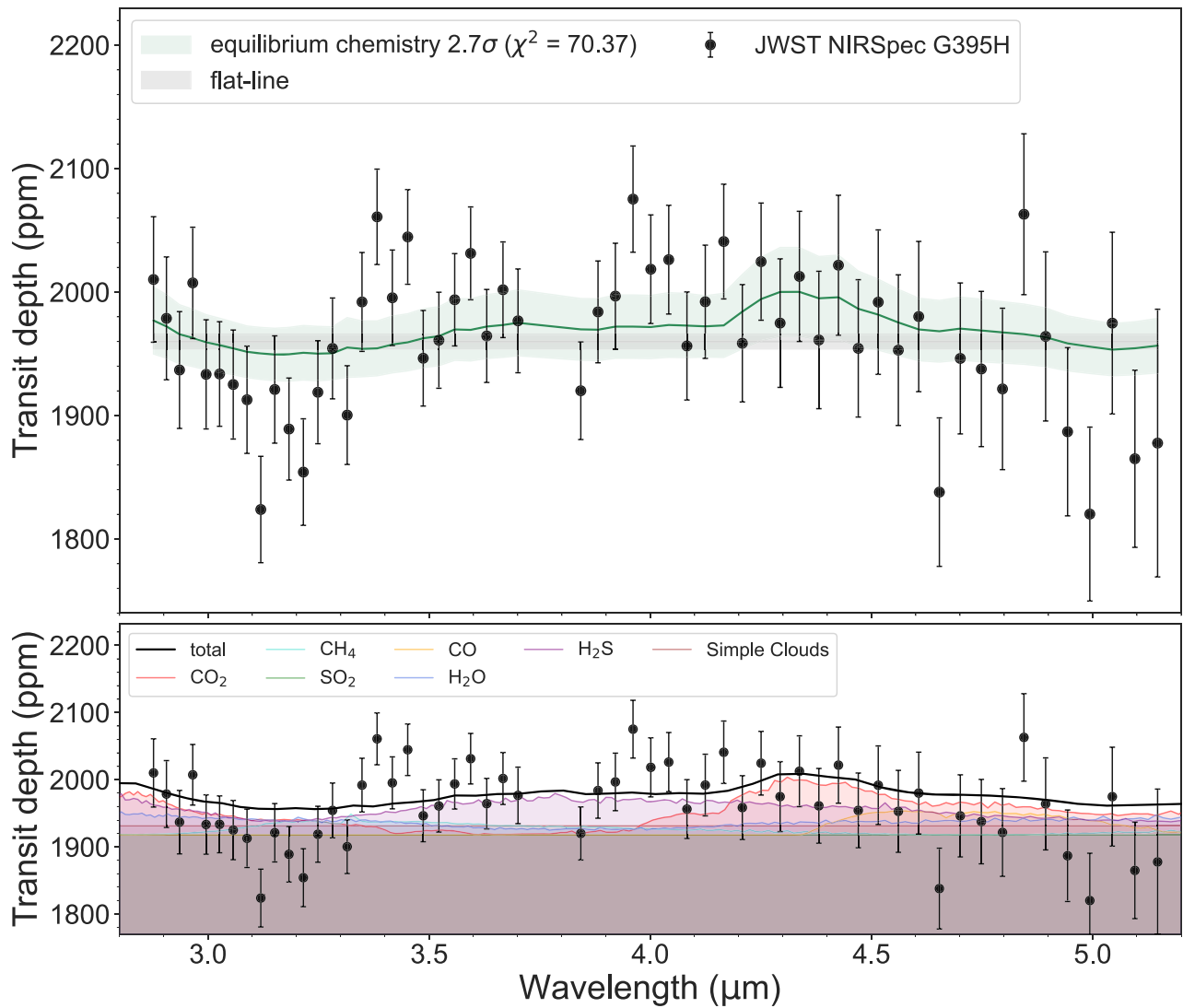


Figure C2. Top panel: transmission spectrum of L98-59 d obtained using transitspectroscopy and binned to $R \sim 100$ (black points) compared to an equilibrium chemistry retrieval model from TauREx (light green). Bottom: opacity contributions from the best-fit model. The model suggests a contribution from H_2S (purple) and CO_2 (red) opacities.

(The data used to create this figure are available in the [online article](#).)

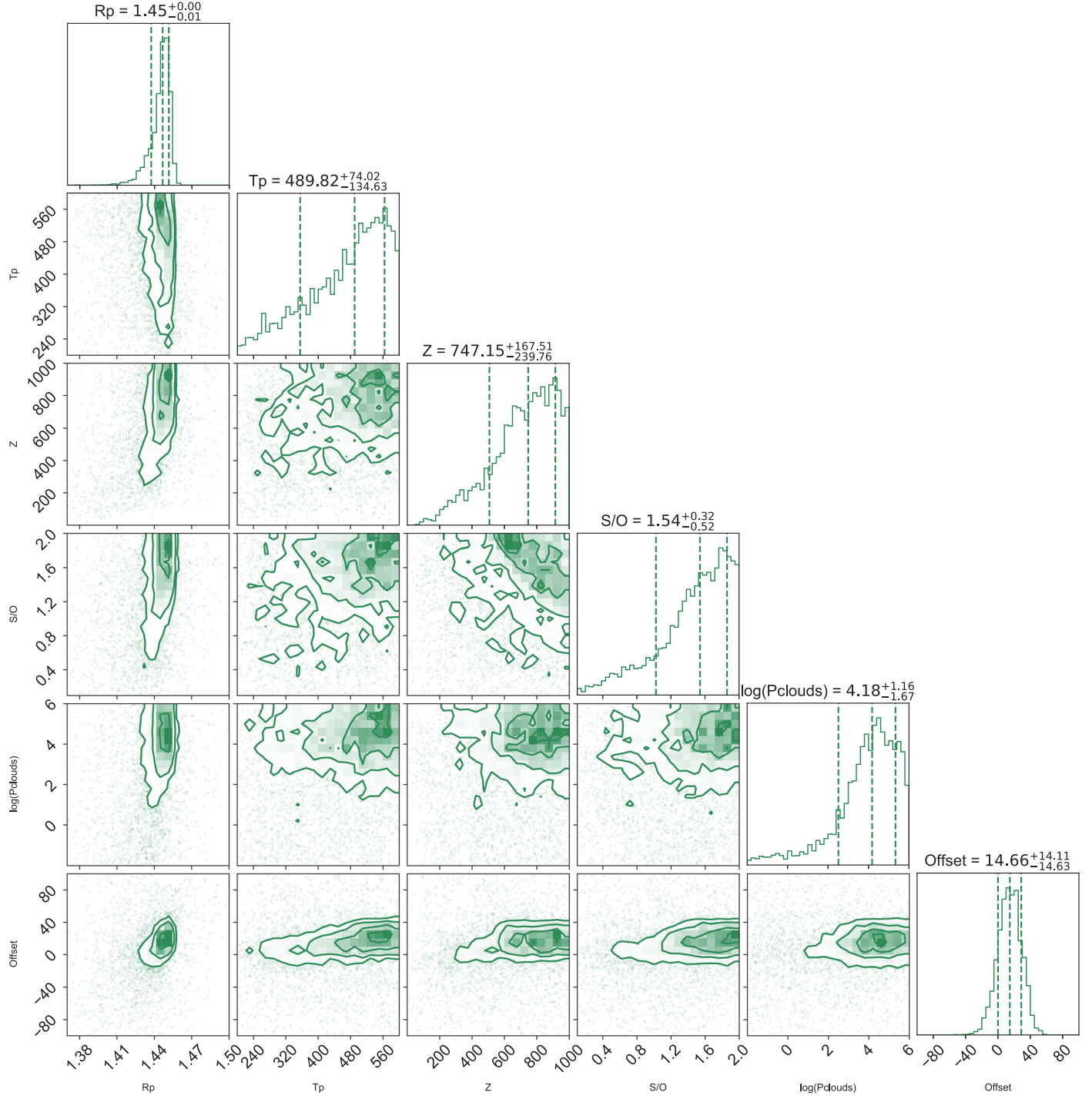


Figure C3. Posterior distributions from the equilibrium chemistry retrieval analysis. Not all parameters in the fit are plotted for clarity.

indicates contributions from H_2S (purple) and CO_2 (red) opacities. The posteriors distributions are in Figure C3.

C.3. Stellar Contamination Retrieval Analysis

We conducted a stellar retrieval analysis and present the posterior distributions obtained in Figure C4. This analysis provides insights into the stellar parameters and their uncertainties. For clarity, not all parameters are plotted, focusing instead on the most relevant distributions.

C.4. Atmospheric Retrieval Analysis on the FIREFLy Data Reduction

To confirm the atmospheric detection, we applied the free chemistry retrieval setup to both the FIREFLy transmission spectrum at $R \approx 100$, $R \approx 100$ and an independent $R \approx 60$, $R \approx 60$ spectrum. While FIREFLy's spectrum appeared flatter, the transitspectroscopy data showed a decrease in transit depths that was well-fitted by H_2S opacity. Sulfur-bearing species remained the primary opacity source in all retrievals. We

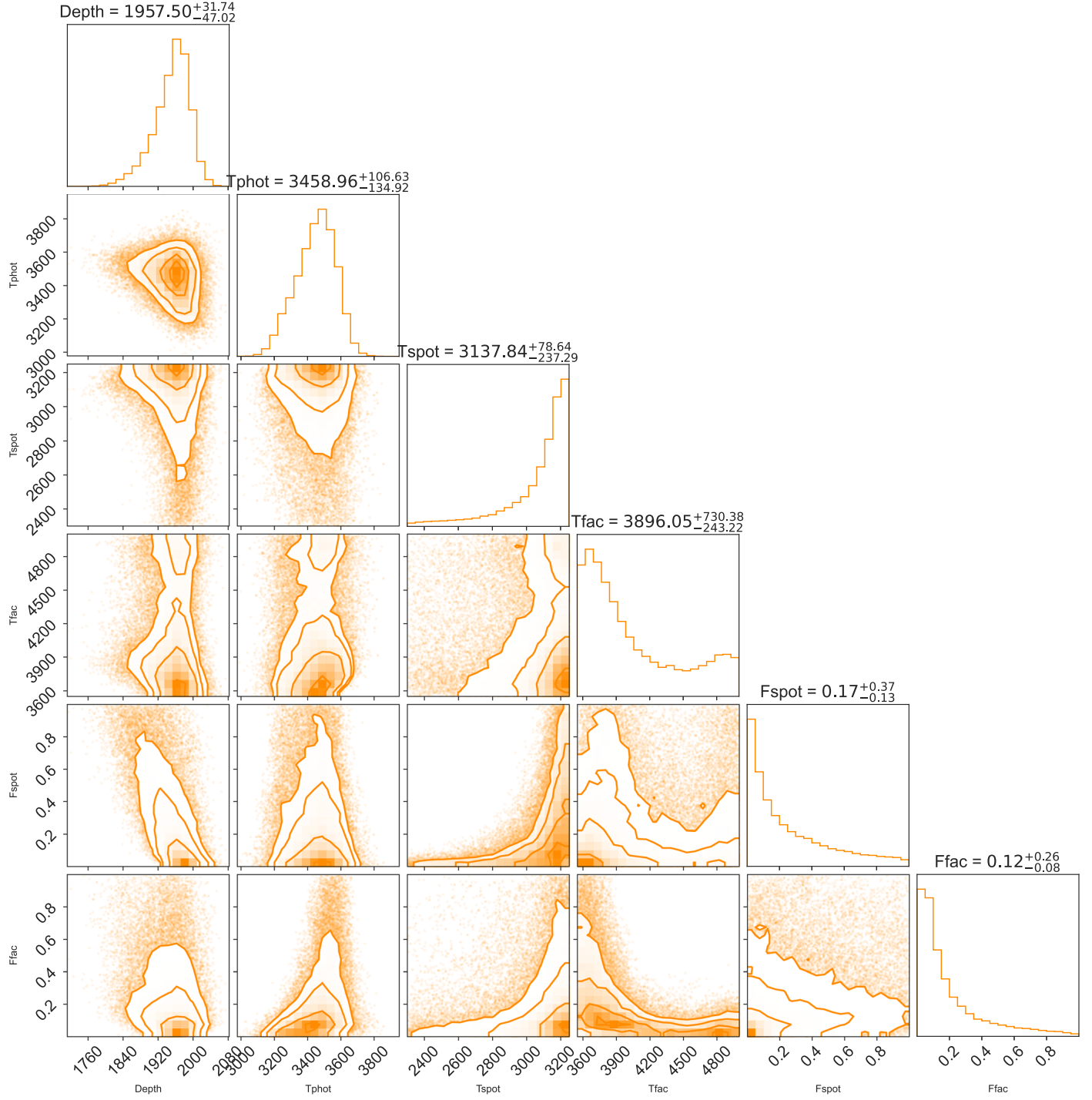


Figure C4. Posterior distributions from the stellar retrieval analysis.

present each spectrum alongside the best-fit atmospheric model and posterior distributions for the relevant parameters.

C.5. Does the Offset between NRS1 and NRS2 Impact the Atmospheric Detection?

To assess the influence of introducing an offset between the NRS1 and NRS2 transit depth values, we conducted an atmospheric retrieval fit on the transmission spectrum of L98-

59 d at $R \sim 100$ obtained from `transitspectroscopy`. The best-fit model is shown in Figure 4 (bottom panel) along with the stellar retrieval model. The atmospheric model is preferred at 3.4σ compared to a flat line with SO_2 and H_2S as the main opacities. Moreover, incorporating these two molecules is favored at a significance of 3.2σ compared to a model without them. Introducing the offset led to higher NRS2 transit depths in `transitspectroscopy`'s data, thereby reinforcing the atmospheric detection, particularly of SO_2 at $4.2 \mu\text{m}$. However,

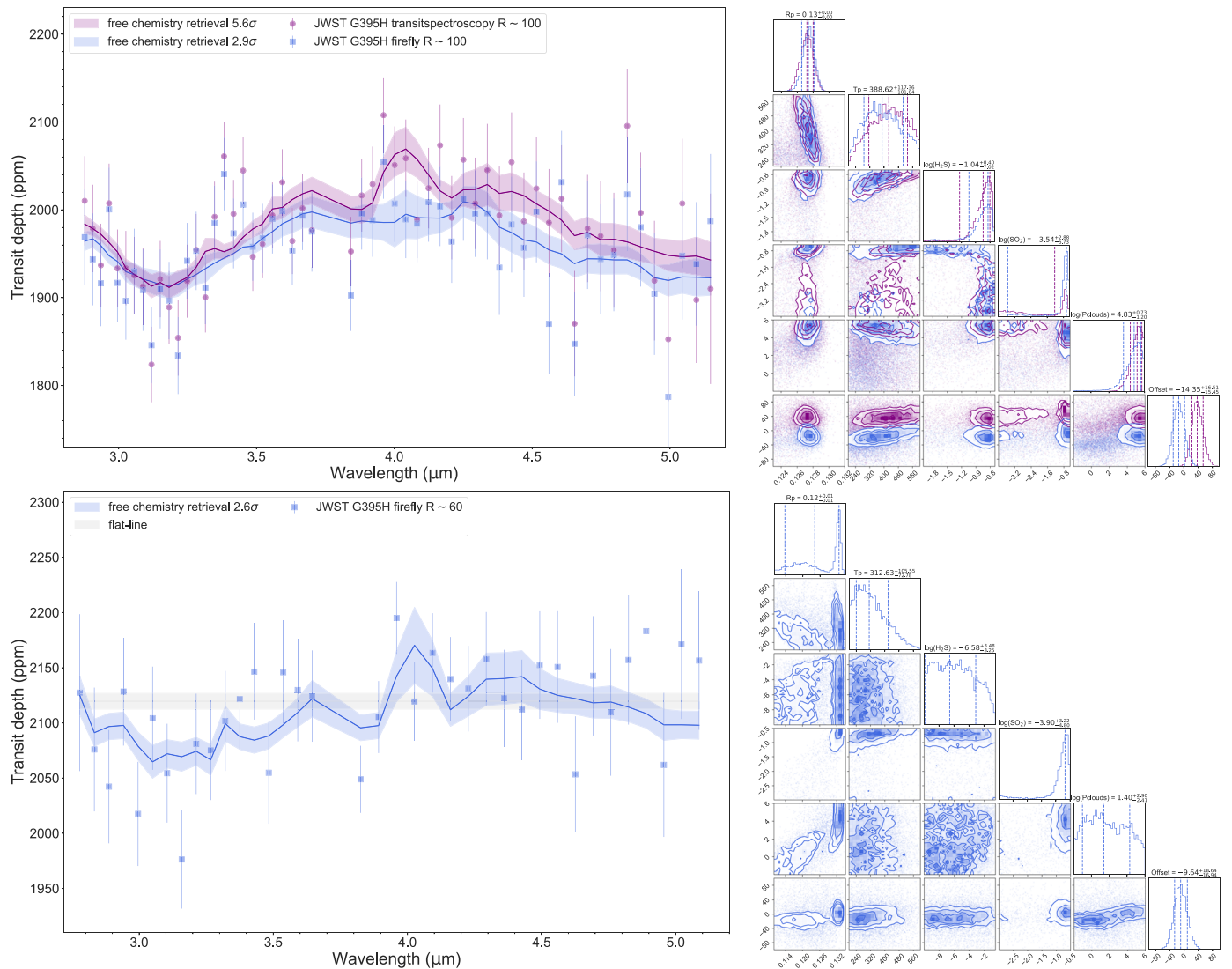


Figure C5. Top left: transmission spectrum of L98-59 d obtained using `transitspectroscopy` (pink data points) and `FIREFLY` (blue data points) and binned to $R \sim 100$ compared to an atmospheric retrieval model with 1σ uncertainty. An offset is fitted between NRS1 and NRS2. Top right: posterior distributions from the atmospheric retrieval analyses. We do not represent all parameters for clarity. The values are printed for the `FIREFLY` atmospheric fit. Bottom left: transmission spectrum of L98-59 d obtained using `FIREFLY` (blue data points) binned to $R \sim 60$ compared to the atmospheric retrieval model with 1σ uncertainty. An offset is fitted between NRS1 and NRS2. Bottom right: posterior distributions from the atmospheric retrieval analysis.

removing the offset did not impact the detection of an atmosphere in `transitspectroscopy`'s reduction.

C.6. Does the Spectral Resolution Impact the Atmospheric Detection?

To examine the impact of spectral resolution on our results, we applied the atmospheric free chemistry retrieval setup to `transitspectroscopy`'s data binned at different resolutions, following the fit at pixel-level resolution. We then evaluated the atmospheric detection by comparing Bayesian evidence with a flat line, representing a fit without opacity sources. We did not fit for an offset between NRS1 and NRS2 in this analysis. The choice of spectral resolution did not significantly affect the atmospheric detection obtained with `transitspectroscopy`'s reduction.

ORCID iDs

- Amélie Gressier <https://orcid.org/0000-0003-0854-3002>
- Néstor Espinoza <https://orcid.org/0000-0001-9513-1449>
- Natalie H. Allen <https://orcid.org/0000-0002-0832-710X>
- David K. Sing <https://orcid.org/0000-0001-6050-7645>
- Agnibha Banerjee <https://orcid.org/0000-0002-9124-6537>
- Joanna K. Barstow <https://orcid.org/0000-0003-3726-5419>
- Jeff A. Valenti <https://orcid.org/0000-0003-3305-6281>
- Nikole K. Lewis <https://orcid.org/0000-0002-8507-1304>
- Stephan M. Birkmann <https://orcid.org/0000-0001-7058-1726>
- Ryan C. Challener <https://orcid.org/0000-0002-8211-6538>
- Elena Manjavacas <https://orcid.org/0000-0003-0192-6887>
- Catarina Alves de Oliveira, <https://orcid.org/0000-0003-2896-4138>
- Nicolas Crouzet <https://orcid.org/0000-0001-7866-8738>
- Tracy. L Beck <https://orcid.org/0000-0002-6881-0574>

References

Al-Refaei, A. F., Changeat, Q., Waldmann, I. P., & Tinetti, G. 2021, *ApJ*, **917**, 37

Alderson, L., Wakeford, H. R., Alam, M. K., et al. 2023, *Natur*, **614**, 664

Ambikasaran, S., Foreman-Mackey, D., Greengard, L., Hogg, D. W., & O’Neil, M. 2015, *ITPAM*, **38**, 252

Azzam, A. A. A., Tennyson, J., Yurchenko, S. N., & Naumenko, O. V. 2016, *MNRAS*, **460**, 4063

Banerjee, A., Barstow, J. K., Gressier, A., et al. 2024, *ApJL*, 975, L11

Barber, R. J., Strange, J. K., Hill, C., et al. 2014, *MNRAS*, **437**, 1828

Baudino, J.-L., Bézard, B., Boccaletti, A., et al. 2015, *A&A*, **582**, A83

Benneke, B., & Seager, S. 2013, *ApJ*, **778**, 153

Benneke, B., Roy, P.-A., Coulombe, L.-P., et al. 2024, arXiv:2403.03325

Birkmann, S. M., Ferruit, P., Giardino, G., et al. 2022, *A&A*, **661**, A83

Blain, D., Charnay, B., & Bézard, B. 2021, *A&A*, **646**, A15

Buchner, J., Georgakakis, A., Nandra, K., et al. 2014, *A&A*, **564**, A125

Charnay, B., Bezard, B., Baudino, J.-L., et al. 2018, *ApJ*, **854**, 172

Chubb, K. L., Tennyson, J., & Yurchenko, S. N. 2020, *MNRAS*, **493**, 1531

Chubb, K. L., Rocchetto, M., Yurchenko, S. N., et al. 2021, *A&A*, **646**, A21

Cloutier, R., Astudillo-Defru, N., Bonfils, X., et al. 2019, *A&A*, **629**, A111

Crossfield, I. J. M. 2023, *ApJL*, **952**, L18

Crossfield, I. J. M., Malik, M., Hill, M. L., et al. 2022, *ApJL*, **937**, L17

Damiano, M., Hu, R., Barclay, T., et al. 2022, *AJ*, **164**, 225

de Wit, J., Wakeford, H. R., Gillon, M., et al. 2016, *Natur*, **537**, 69

de Wit, J., Wakeford, H. R., Lewis, N. K., et al. 2018, *NatAs*, **2**, 214

Demangeon, O. D. S., Zapatero Osorio, M. R., Alibert, Y., et al. 2021, *A&A*, **653**, A41

Demory, B.-O., Gillon, M., Madhusudhan, N., & Queloz, D. 2015, *MNRAS*, **455**, 2018

Demory, B.-O., Gillon, M., Seager, S., et al. 2012, *ApJ*, **751**, L28

Demory, B.-O., Gillon, M., Deming, D., et al. 2011, *A&A*, **533**, A114

Demory, B.-O., Gillon, M., de Wit, J., et al. 2016, *Natur*, **532**, 207

Diamond-Lowe, H., Berta-Thompson, Z., Charbonneau, D., & Kempton, E. M.-R. 2018, *AJ*, **156**, 13

Dyre, A., Min, M., Decin, L., et al. 2024, *Natur*, **625**, 51

Edwards, B., Changeat, Q., Mori, M., et al. 2021, *AJ*, **161**, 44

Espinosa, N., 2022 *TransitSpectroscopy*, v0.3.11, Zenodo, doi: [10.5281/zenodo.6960924](https://doi.org/10.5281/zenodo.6960924)

Espinosa, N., Kossakowski, D., & Brahm, R. 2019, *MNRAS*, **490**, 2262

Feinstein, A. D., Radica, M., Welbanks, L., et al. 2023, *Natur*, **614**, 670

Feroz, F., Hobson, M. P., & Bridges, M. 2009, *MNRAS*, **398**, 1601

Foreman-Mackey, D., Agol, E., Ambikasaran, S., & Angus, R. 2017, *AJ*, **154**, 220

Garcia, L. J., Moran, S. E., Rackham, B. V., et al. 2022, *A&A*, **665**, A19

Grant, D., & Wakeford, H. R. 2022, *Exo-TiC/ExoTiC-LD: ExoTiC-LD v3.0.0*, Zenodo, doi: [10.5281/zenodo.7437681](https://doi.org/10.5281/zenodo.7437681)

Greene, T. P., Bell, T. J., Ducrot, E., et al. 2023, *Natur*, **618**, 39

Greene, T. P., Line, M. R., Montero, C., et al. 2016, *ApJ*, **817**, 17

Gressier, A., Mori, M., Changeat, Q., et al. 2022, *A&A*, **658**, A133

Holmberg, M., & Madhusudhan, N. 2024, *A&A*, **683**, L2

Hu, R., Seager, S., & Bains, W. 2013, *ApJ*, **769**, 6

Hu, R., Bello-Arufe, A., Zhang, M., et al. 2024, *Natur*, **630**, 609

Husser, T.-O., Wende-von Berg, S., Dreizler, S., et al. 2013, *A&A*, **553**, A6

Irwin, P. G. J., Teanby, N. A., de Kok, R., et al. 2008, *JQSRT*, **109**, 1136

Jakobsen, P., Ferruit, P., Alves de Oliveira, C., et al. 2022, *A&A*, **661**, A80

Janssen, L. J., Woitke, P., Herbst, O., et al. 2023, *AN*, **344**, e20230075

Kipping, D. M. 2013, *MNRAS*, **435**, 2152

Kirk, J., Stevenson, K. B., Fu, G., et al. 2024, *AJ*, **167**, 90

Kostov, V. B., Schlieder, J. E., Barclay, T., et al. 2019, *AJ*, **158**, 32

Kreidberg, L., Koll, D. D. B., Morley, C., et al. 2019, *Natur*, **573**, 87

Li, G., Gordon, I. E., Rothman, L. S., et al. 2015, *ApJS*, **216**, 15

Lim, O., Benneke, B., Doyon, R., et al. 2023, *ApJL*, **955**, L22

Lodders, K. 2010, in *Principles and Perspectives in Cosmochemistry, Astrophysics and Space Science Proc.*, 16, ed. A. Goswami & B. E. Reddy (Berlin: Springer), 379

Luque, R., & Palle, E. 2022, *Sci*, **377**, 1211

Lustig-Yaeger, J., Fu, G., May, E. M., et al. 2023, *NatAs*, **7**, 1317

Madhusudhan, N., Sarkar, S., Constantinou, S., et al. 2023, *ApJ*, **956**, L13

Mant, B. P., Yachmenev, A., Tennyson, J., & Yurchenko, S. N. 2018, *MNRAS*, **478**, 3220

May, E. M., MacDonald, R. J., Bennett, K. A., et al. 2023, *ApJL*, **959**, L9

McKemmish, L. K., Masseron, T., Hoeijmakers, H. J., et al. 2019, *MNRAS*, **488**, 2836

McKemmish, L. K., Yurchenko, S. N., & Tennyson, J. 2016, *MNRAS*, **463**, 771

Moran, S. E., Horst, S. M., Batalha, N. E., Lewis, N. K., & Wakeford, H. R. 2018, *AJ*, **156**, 252

Moran, S. E., Stevenson, K. B., Sing, D. K., et al. 2023, *ApJL*, **948**, L11

Morley, C. V., Fortney, J. J., Marley, M. S., et al. 2012, *AJ*, **156**, 172

Mugnai, L. V., Modirrousta-Galian, D., Edwards, B., et al. 2021, *AJ*, **161**, 284

Owen, J. E. 2019, *AREPS*, **47**, 67

Owen, J. E., & Wu, Y. 2013, *ApJ*, **775**, 105

Polman, J., Waters, L. B. F. M., Min, M., Miguel, Y., & Khorshid, N. 2023, *A&A*, **670**, A161

Polyansky, O. L., Kyuberis, A. A., Zobov, N. F., et al. 2018, *MNRAS*, **480**, 2597

Powell, D., Feinstein, A. D., Lee, E. K. H., et al. 2024, *Natur*, **626**, 979

Rackham, B. V., Apai, D., & Giampapa, M. S. 2018, *ApJ*, **853**, 122

Rogers, J. G., Gupta, A., Owen, J. E., & Schlichting, H. E. 2021, *MNRAS*, **508**, 5886

Rogers, L. A. 2015, *ApJ*, **801**, 41

Rothman, L. S., Gamache, R. R., Goldman, A., et al. 1987, *ApOpt*, **26**, 4058

Rothman, L. S., Gordon, I. E., Barber, R. J., et al. 2010, *JQSRT*, **111**, 2139

Rustamkulov, Z., Sing, D. K., Liu, R., & Wang, A. 2022, *ApJL*, **928**, L7

Rustamkulov, Z., Sing, D. K., Mukherjee, S., et al. 2023, *Natur*, **614**, 659

Speagle, J. S. 2020, *MNRAS*, **493**, 3132

Tennyson, J., & Yurchenko, S. N. 2018, *Atoms*, **6**, 26

Tennyson, J., Yurchenko, S. N., Al-Refaei, A. F., et al. 2016, *JMoSp*, **327**, 73

Trotta, R. 2008, *ConPh*, **49**, 71

Tsai, S.-M., Lee, E. K. H., Powell, D., et al. 2023, *Natur*, **617**, 483

Underwood, D. S., Tennyson, J., Yurchenko, S. N., et al. 2016, *MNRAS*, **459**, 3890

Wakeford, H. R., Lewis, N. K., Fowler, J., et al. 2019, *AJ*, **157**, 11

Woitke, P., Helling, C., Hunter, G. H., et al. 2018, *A&A*, **614**, A1

Yang, J., Irwin, P. G. J., & Barstow, J. K. 2023, *MNRAS*, **525**, 5146

Yurchenko, S. N., Amundsen, D. S., Tennyson, J., & Waldmann, I. P. 2017, *A&A*, **605**, A95

Yurchenko, S. N., Barber, R. J., & Tennyson, J. 2011, *MNRAS*, **413**, 1828

Yurchenko, S. N., Tennyson, J., Syme, A.-M., et al. 2021, *MNRAS*, **510**, 903

Zahnle, K. J., & Marley, M. S. 2014, *ApJ*, **797**, 41

Zhou, L., Ma, B., Wang, Y.-H., & Zhu, Y.-N. 2023, *RAA*, **23**, 025011

Zieba, S., Zilinskas, M., Kreidberg, L., et al. 2022, *A&A*, **664**, A79

Zieba, S., Kreidberg, L., Ducrot, E., et al. 2023, *Natur*, **620**, 746